A first-in-human study of quantitative ultrasound to assess transplant kidney fibrosis

Eno Hysi[1,2,3,4], Jihye Baek[5,9], Alexander Koven [2,3,6,9], Xiaolin He[2,3,7], Luisa Ulloa Severino[2,3,7], Yiting Wu[2,3,7], Kendrix Kek [2,3,7], Shukai Huang[2,3,7], Adriana Krizova[8], Monica Farcas[2,3,6], Michael Ordon[6], Kai-Ho Fok[6], Robert Stewart[6], Kenneth T. Pace [6], Michael C. Kolios [2,3,4,10], Kevin J. Parker [5,10] & Darren A. Yuen [2,3,7,10] ✉

Kidney transplantation is the optimal treatment for renal failure. In the United States, a biopsy at the time of organ procurement is often used to assess kidney quality to decide whether it should be used for transplant. This assessment is focused on renal fibrotic burden, because fibrosis is an important measure of irreversible kidney injury. Unfortunately, biopsy at the time of transplant is plagued by problems, including bleeding risk, inaccuracies introduced by sampling bias and rapid sample preparation, and the need for round-the-clock pathology expertise. We developed a quantitative algorithm, called renal H-scan, that can be added to standard ultrasound workflows to quickly and noninvasively measure renal fibrotic burden in preclinical animal models and human transplant kidneys. Furthermore, we provide evidence that biopsy-based fibrosis estimates, because of their highly localized nature, are inaccurate measures of whole-kidney fibrotic burden and do not associate with kidney function post-transplant. In contrast, we show that whole-kidney H-scan fibrosis estimates associate closely with post-transplant renal function. Taken together, our data suggest that the addition of H-scan to standard ultrasound workflows could provide a safe, rapid and easy-to-perform method for accurate quantification of transplant kidney fibrotic burden, and thus better prediction of post-transplant renal outcomes.

Kidney transplantation improves the survival and quality of life for people with end-stage kidney disease. However, the demand for kidneys vastly outstrips the supply of available donors. As of December 2023, over 93,000 patients were waiting for a kidney transplant in the United States alone[1], leading to a median wait time of roughly 4 years[1–3]. In an effort to address this marked supply–demand imbalance, clinicians have progressively loosened the criteria for donor selection to include older donors and/or those with pre-existing health conditions that might adversely impact donor kidney quality. In an effort to categorize donor kidneys based on their presumed quality, the kidney donor risk index (KDRI) was developed and validated in 2009 (ref. 4). In this system, which was officially implemented in 2013, each deceased donor is assigned a KDRI, and a corresponding kidney donor profile index (KDPI) score that ranges from 0 to 100%, with higher KDPI scores generally reflecting poorer-quality kidneys. KDPI scores are indexed to kidneys recovered in the previous calendar year in the United States, and thus

a KDPI of 85% means that the donor kidney has a higher expected risk of graft failure than 85% of all donor kidneys recovered in the previous year. Given this increased graft failure risk, receipt of a donor kidney with a KDPI score >85% in the United States requires that patients provide special informed consent[5]. Not surprisingly, individuals who receive kidneys from donors with KDPI >85% have poorer renal outcomes, on average[6–8], compared with those receiving kidneys with KDPI ≤85%. However, the distinction between KDPI >85% and ≤85% kidneys remains imprecise, with some KDPI >85% kidneys having an average healthy lifespan that exceeds that of kidneys with lower KDPI scores[4,7–9]. Likewise, although a KDPI ≤85% kidney on average lasts longer than those with KDPI >85%, some KDPI ≤85% kidneys progress to end-stage kidney disease due to occult donor-derived disease[4,7–9]. Given this imprecision, kidney biopsies are often performed in the United States at the time of procurement, with histologic analysis of chronic donor-derived renal injury, such as scarring, used to further assess donor kidney quality[10]. Unfortunately, this histologic analysis does not appear to improve transplant outcomes and may increase kidney discard rates[11]. New tools are required to better estimate kidney quality and more accurately predict transplant kidney outcomes.

Fibrosis is one of the most common and important forms of chronic kidney damage. Fibrotic injury arises when healthy kidney tissue is replaced with a pathologic matrix that also destroys and damages renal capillaries, impairing tissue perfusion and oxygenation and, ultimately, causing progressive loss of kidney function[12]. Fibrotic burden is thus a powerful marker of irreversible renal damage and an important predictor of ongoing kidney injury and, therefore, renal lifespan[13]. As such, the ability to accurately measure donor-derived fibrotic burden could have major implications on how donor kidney selection and allocation are performed.

Currently, clinicians have a limited ability to assess kidney fibrotic burden[14]. Because no clinical parameters correlate closely with renal fibrosis, the only way to measure scarring currently is via a kidney biopsy and subsequent histopathologic assessment. Such evaluations are not ideal because they can increase the risk of post-transplant bleeding, are often suboptimal because they require rapid staining of frozen tissue sections, sample only <1% of the kidney volume and require expert pathologic assessment at all times of the day and night[15–17].

Ultrasound is a noninvasive, widely available modality that does not require nephrotoxic contrast agents and that can rapidly image the entire kidney[18,19]. Although useful for identification of structural abnormalities such as urinary obstruction, perinephric fluid collections and large-vessel stenosis or thrombosis[20], traditional ultrasound imaging is currently unable to visualize microscopic processes such as fibrosis[21]. One major limitation preventing the use of ultrasound as a way to image fibrosis has been its historical reliance on the signal amplitude of conventional grayscale images[22]. Changes in brightness levels in an ultrasound image can occur for a wide variety of reasons unrelated to fibrosis[23], making it impossible to accurately detect and quantify scar tissue, which is microscopic in nature and spatially diffuse. However, underlying tissue microstructure within ultrasound datasets can be characterized by analysis of the raw radiofrequency (RF) signals used to generate conventional ultrasound images[24–27]. Unlike grayscale images, RF signals encode information about the underlying microscopic tissue structure, which is otherwise not visible[28]. We have previously shown that quantitative analysis of RF signals (broadly known as quantitative

ultrasound[26]) can detect changes in liver tissue structure induced by experimental liver fibrosis in rodents[29–32]. Here, we generated an ultrasound image analysis algorithm for assessment of experimental murine kidney fibrosis, then refined it for measurement of scar burden in human nephrectomy samples. This algorithm, called renal H-scan, is sensitive to the size of scattering microstructures in the imaged tissue, with larger scatterers depicted as red pixels, corresponding to increasing amounts of fibrosis. We also validated our renal H-scan algorithm in a first-in-human experiment, demonstrating an outstanding correlation between H-scan estimates and gold standard histologic measures of fibrotic burden in human kidneys undergoing transplantation. Importantly, unlike localized biopsy-based fibrotic estimates, which did not predict post-transplant kidney function, whole-kidney H-scan fibrosis measurements corresponded with renal function 1 year post-transplant. Taken together, our data show the potential of renal H-scan as a way to quickly and accurately monitor donor kidney fibrotic burden and thus potentially aid in donor organ selection.

Results

H-scan accurately tracks mouse kidney fibrosis progression

To first assess the ability of renal H-scan to quantify kidney fibrosis, we used the unilateral ureteral obstruction (UUO) mouse model to induce progressive kidney fibrosis, which develops over the course of 14 days (Extended Data Fig. 1a,b). Although conventional B-mode ultrasound imaging of mouse kidneys 7 and 14 days post-UUO detected progressive dilation of the renal pelvis and calyces (Extended Data Fig. 1c), no obvious differences in renal cortical tissue were noted on B-mode images when compared with healthy sham-operated kidneys. In contrast, H-scan imaging of the kidney demonstrated a progressive increase in the number of large ultrasound scatterers (visualized as red pixels on H-scan images) in the fibrotic left kidney of UUO mice over the course of 14 days, reflecting increased matrix deposition (Extended Data Fig. 1d). Analysis of only the outer kidney region (cortex) and the inner region (medulla) demonstrated similar increases in H-scan percentage red pixel content (Extended Data Fig. 1d,e). Extended Data Fig. 1e shows quantification of fibrotic H-scan red pixel content in kidneys from the sham group compared with days 7 and 14 UUO kidneys. In line with our H-scan findings, gold standard histologic fibrosis measurements, as assessed by picrosirius red (PSR), collagen I and α-smooth muscle actin (α-SMA) staining, demonstrated a similar rise in fibrotic burden over the course of 14 days (Extended Data Fig. 1f–h). Importantly, H-scan percentage red pixel density correlated tightly with these gold standard histology-based measurements of renal fibrosis (Extended Data Fig. 1i–k), indicating that H-scan can accurately quantify experimental murine kidney fibrosis and its progression over time (all correlations ≥0.91 for whole kidney and outer and inner regions of interest).

Human nephrectomy fibrosis can be quantified using H-scan

We next scanned a set of human kidney specimens collected from five clinically indicated radical nephrectomy surgeries, to test whether we could replicate our murine findings in human kidney tissue (Fig. 1a,b). Although H-scan imaging demonstrated considerable inter- and intrasample heterogeneity in percentage red pixel density (for estimation of of renal fibrotic burden, see Fig. 1c–e), our H-scan-based fibrosis estimates again correlated tightly with gold standard histology assessments (Fig. 1f–i).

Fig. 1 | H-scan analysis of human nephrectomy specimens. a, Schematic of human nephrectomy imaging study. Portions of human kidney cortex removed during radical nephrectomy were scanned, from left to right. **b,c**, Representative B-mode (**b**) and H-scan images (**c**) of the five specimens ordered by increasing overall fibrotic burden (scale bars, 5 mm). **d**, H-scan pixel histograms showing the percentage of red pixels (larger scatterers) and blue (smaller scatterers) pixels in each specimen. **e**, A motor moved the ultrasound probe at 150-μm increments from left to right, thus providing a three-dimensional (3D) assessment of fibrotic

burden. **f,g**, Representative PSR- (**f**) and Masson trichrome-stained sections (**g**) from each of the five specimens (scale bars, 100 μm). Renal fibrotic burden was then estimated using gold standard histologic quantification of both PSR- and Masson trichrome-stained sections. **h,i**, Correlations between H-scan percentage red fibrosis values and gold standard histologic measurements of fibrosis, as assessed by PSR (**h**) and Masson trichrome staining (**i**). Pearson correlation coefficients (*r*) and corresponding *P* values are shown. **a** created with BioRender.com.
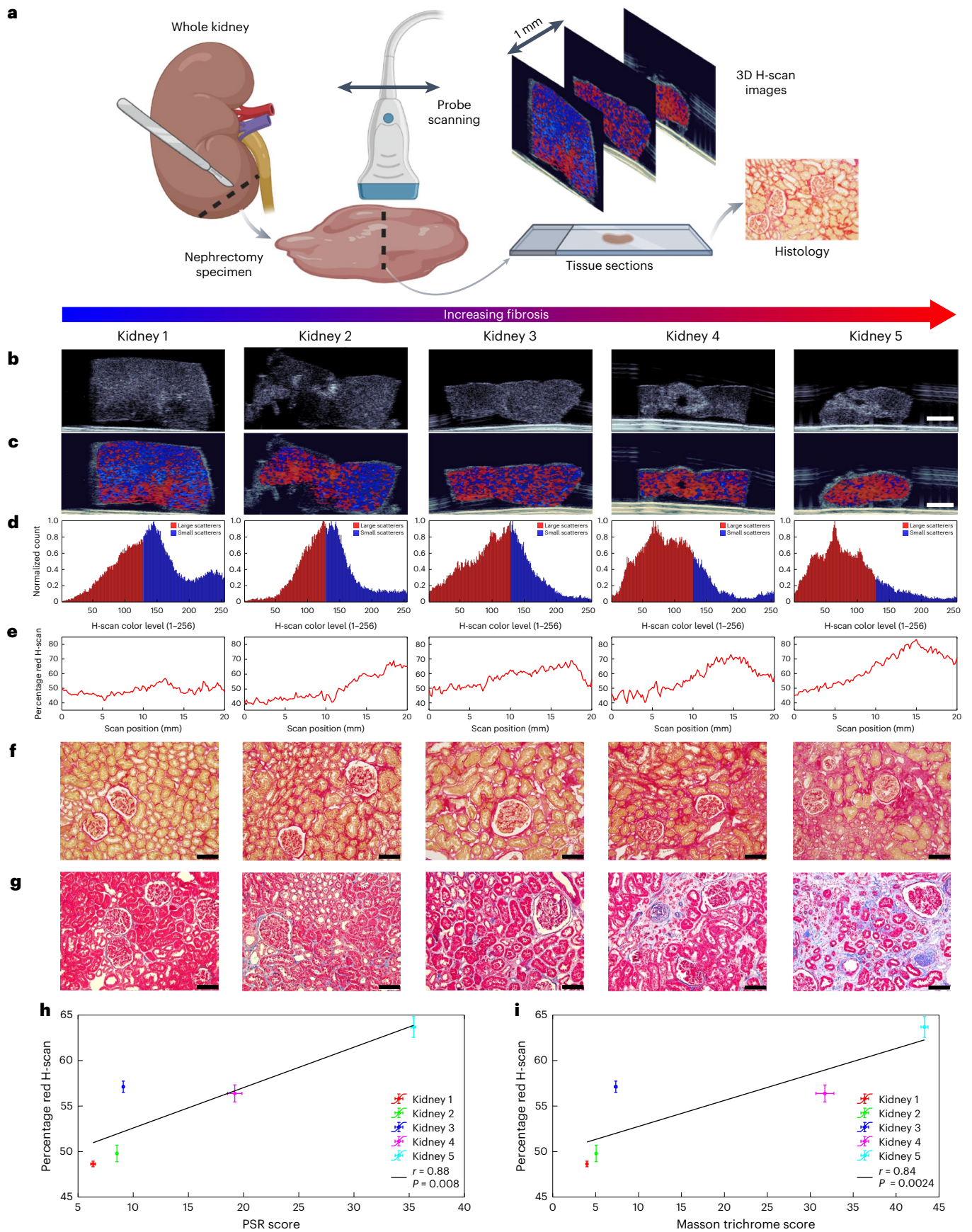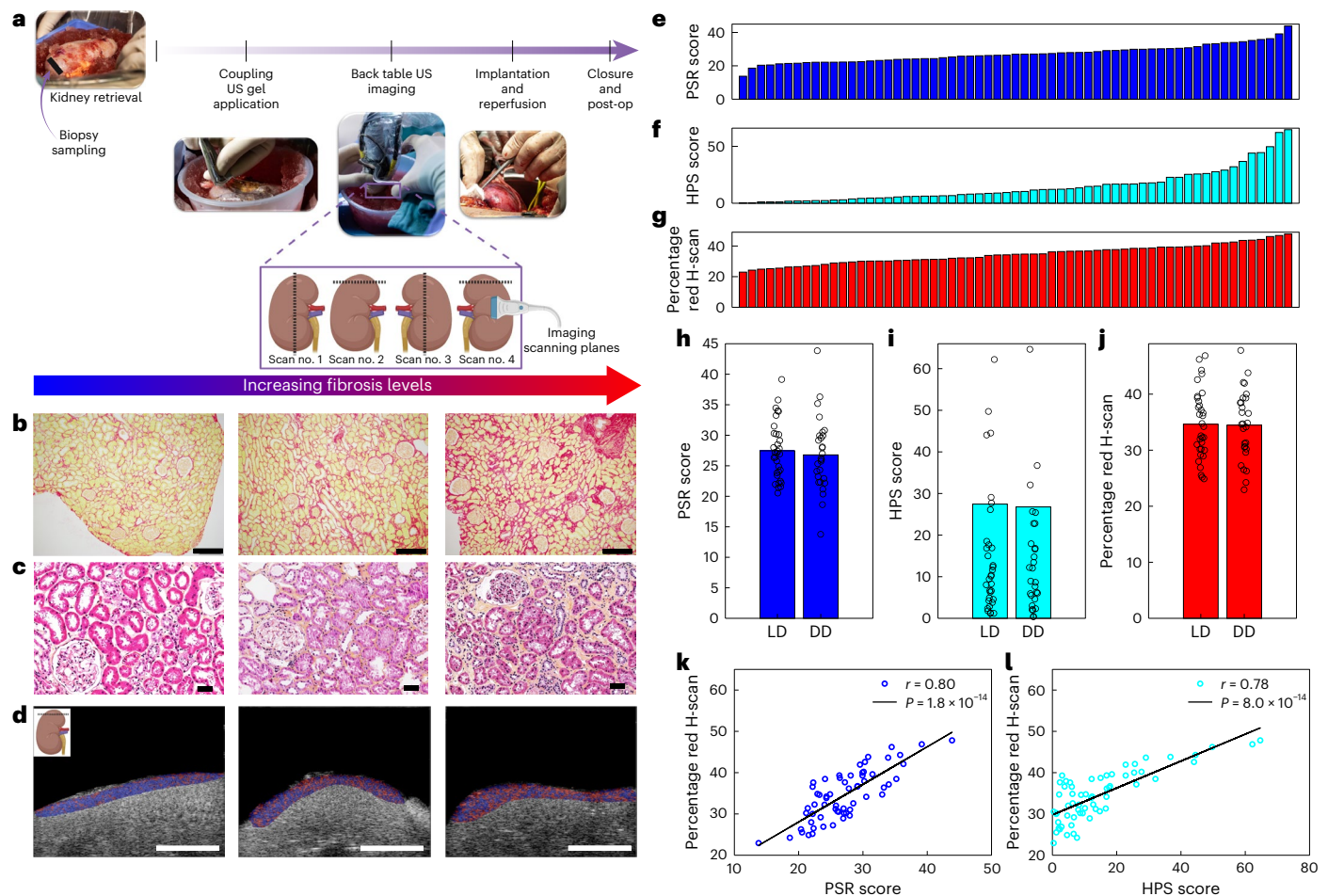
Fig. 2 | H-scan of human transplant kidneys. a, Schematic of a first-in-human transplant kidney H-scan imaging study. Kidneys were scanned in two longitudinal planes along the longest axis of the kidney, from opposing sides (scan nos. 1 and 3) and in two transverse planes at the biopsy site in a similar fashion (scan nos. 2 and 4). **b–d**, Representative PSR- (**b**) and HPS-stained sections (**c**) and H-scan images (**d**) of a subcapsular cortex region of interest performed at the biopsy site (scan no. 2 for the US imaging plane). Scale bars: 500 μm (**b**), 50 μm (**c**) and 10 mm (**d**). **e–g**, Quantification of PSR (**e**), HPS (**f**) and H-scan images (**g**) for all 61 donor kidneys, ordered by increasing stain/H-scan percentage red levels, with each bar representing a patient enrolled in the study.

h–j, Comparison of DD and LD biopsy site fibrotic burden as assessed by PSR (**h**), HPS (**i**) and H-scan (**j**). For comparison of LD and DD, an independent samples *t*-test was performed, revealing no statistical significance between the groups, with the the following test statistics: PSR ($P = 0.63$, $F = 0.24$, 95% confidence interval (CI) [−2.07, 3.42], $\eta = 0.0075$); HPS ($P = 0.80$, $F = 0.059$, 95% CI [−6.65, 8.49], $\eta = 0.0018$); and H-scan ($P = 0.92$, $F = 0.011$, 95% CI [−2.99, 3.31], $\eta = 0.0030$). **k,l**, Correlations between H-scan scores derived from biopsy site subcapsular cortex ROI with PSR (**k**) and HPS (**l**) histological staining of the same region. Pearson correlation coefficients (*r*) and corresponding *P* values are shown. **a** created with BioRender.com.

Human transplant kidney fibrosis assessment using H-scan

To determine whether we could utilize renal H-scan in a clinical setting, we next conducted a first-in-human clinical experiment of this imaging technique in human donor kidneys intended for transplantation (Fig. 2a). A total of 61 donor kidneys were imaged, from 28 deceased donors (DD) and 33 living donors (LD). Each kidney was transplanted into a unique recipient, and thus 61 recipients were enrolled in the trial. Recipient and donor demographic and clinical characteristics are summarized in Tables 1 and 2, respectively. Mean warm ischemia time (±s.d.) for all kidneys was 37 ± 7 min, and mean cold ischemia time for deceased donor kidneys was 549 ± 191 min.

Sections from donor kidney wedge biopsy samples were stained to estimate fibrotic burden (Fig. 2b,c), and each kidney was scanned post-biopsy (Fig. 2d). We noted considerable heterogeneity in matrix deposition within and between kidney biopsies, with up to 30 and 60% variation, respectively, in PSR and hematoxylin phloxin saffron (HPS) measurements of fibrotic burden across the 61 donor kidneys (Fig. 2e,f).

Renal H-scanning of each kidney lasted on average 5 min and could be performed by both resident and staff surgeons with minimal training

(Fig. 2d,g). Because of the marked intrarenal spatial heterogeneity that we had observed in our previous analyses (Fig. 1), we first focused our attention on renal H-scans of subcapsular cortex at the biopsy site (Fig. 2d,g). Interestingly, both renal H-scan and histologic measurements indicated that the fibrotic burden in living donor kidneys was similar to that of deceased donors (Fig. 2h–j). Importantly, these spatially c-localized analyses demonstrated a strong correlation between renal H-scan estimates and gold standard histologic measurements of renal fibrotic burden (Fig. 2k,l).

Because fibrosis is often heterogeneously distributed throughout the kidney[33,34], we next hypothesized that H-scans of larger regions of interest (ROIs) that included more tissue outside of the biopsy site would be less strongly correlated with the highly localized, biopsy-based histologic estimates of fibrotic burden. To answer this question, we compared our histologic fibrosis measurements from the biopsy site (containing only subcapsular cortex) with renal H-scan values from the entire depth of the kidney (cortex and medulla) at the biopsy site (Fig. 3a). This analysis was carried out also when either the cortex (Fig. 3b) or both cortex and medulla were imaged away from

Table 1 | Recipient characteristics

Characteristics	Values
Number of recipients	61
Age (years)	55.5±11.4
Gender (% female)	45.9
Height (cm)	166.5±15.2
Weight at time of transplant (kg)	81.4±22.8
Initial cause of end-stage renal disease (no. of recipients)	Diabetes mellius: 11
	Glomerulonephritis: 20
	Hypertension: 2
	Interstitial nephritis: 3
	Polycystic kidney disease: 9
	Congenital: 1
	Other/unknown: 15
Type of dialysis pretransplant: % (no. of recipients)	Hemodialysis: 63.9 (39)
	Peritoneal dialysis: 19.7 (12)
	None/predialysis: 16.4 (10)
Time on dialysis pretransplant (years)	3.7±2.5
Induction immunosuppression (no. of recipients)	Basiliximab: 55
	Antithymocyte globulin: 5
	Unknown: 1
Maintenance immunosuppression medication (% recipients)	Calcineurin inhibitor: 58
	Mycophenolate: 51
	Azathioprine: 1
	Prednisone: 59
	Sirolimus: 1

All values are mean±s.d. unless otherwise noted.

Table 2 | Transplant kidney and donor characteristics

Characteristics	Values
Donor age (years)	45.5±14.1
Gender: % female (no. of donors)	54.1 (33 female, 28 male)
	Deceased donors (14 female, 14 male)
	Living donors (19 female, 14 male)
Height (cm)	169.1±9.7
Weight at time of transplant (kg)	77.2±16.7
Self/family-reported ethnicity: % (no. of donors)	Asian: 6.6 (4)
	Black or African American: 1.6 (1)
	Hispanic: 1.6 (1)
	White: 55.8 (34)
	Other: 21.3 (13)
	Unknown: 13.1 (8)
Past medical history: % (no. of patients)	**Hypertension**
	No: 83.6 (51)
	Unkown: 6.6 (4)
	Yes: 9.8 (6)
	Diabetes
	No: 93.4 (57)
	Unknown: 4.9 (3)
	Yes: 1.6 (1)
Cause of death: % (no. of patients)	Anoxia: 32.1 (9)
	Cerebrovascular/stroke: 35.7 (10)
	Head trauma: 14.3 (4)
	Other: 10.7 (3)
	CNS tumor: 0 (0)
	Unknown: 7.1 (2)
Donor type (%)	LD: 54.1 (33/61)
	DD: 45.9 (28/61)
	NDD: 32.8 (20/61)
	DCD: 13.1 (8/61)
Donor terminal serum creatinine at time of procurement (µmol l⁻¹)	All donors: 70.5±38.9
	LD: 71.5±15.9
	DD: 69.4±55.4
Donor terminal CKD-EPI 2021 eGFR (ml min⁻¹)	102.9±23.7
	LD: 101.1±15.0
	DD: 105.0±31.3
KDPI for DD	44.1±27.5
Total cold ischemia time (min)	549±191
Total warm ischemia time (min)	37±7

All values are mean±s.d. unless otherwise noted. CKD-EPI, Chronic Kidney Disease Epidemiology Collaboration 2021; CNS, central nervous system; DCD, donation following cardiac death; NDD, neurological determinant of death.

the biopsy site, using a longitudinal imaging plane (Fig. 3c). As shown in Fig. 3a and Extended Data Fig. 2a, a renal H-scan of both the cortex and medulla at the biopsy site still positively correlated with histologic estimation, although the correlation was weaker than when only the actual site of the biopsy (the cortex) was imaged (Fig. 2k,l). Similarly, both cortical (Fig. 3b and Extended Data Fig. 2b) and full-thickness (Fig. 3c and Extended Data Fig. 2c) H-scans taken away from the biopsy site, along the longitudinal axis of the kidney, demonstrated even weaker correlations with biopsy-based histologic analyses.

H-scan results associate with renal function post-transplant

Given the importance of fibrosis as a marker of chronic injury, we next hypothesized that H-scan estimates of donor-derived renal fibrotic burden would associate with kidney function post-transplant. At study end, 53 patients ($n = 29$ LD, $n = 24$ DD) had reached a minimum of 12 months post-transplant. The mean estimated glomerular filtration rate (eGFR) in these 53 patients was $60 ± 21$ ml min⁻¹ 1.73 m⁻² body surface area at 9–12 months post-transplant. As expected, living donor kidney transplant recipients had a higher eGFR when compared with deceased donor kidney recipients (Fig. 4a; $P < 0.05$). Among deceased donor kidney recipients, those who received KDPI ≤85% kidneys ($n = 21$) had, on average, better renal function compared with KDPI >85% kidney recipients ($n = 3$, $P < 0.05$; Fig. 4b). Interestingly, whole-kidney H-scan fibrosis estimates were negatively associated with eGFR at 9–12 months post-transplant ($r = -0.53$, $P = 0.00004$), with a stepwise decline in kidney function noted with increasing H-scan quartile (Fig. 4c).

By contrast, standard histologic fibrosis measurements, including interstitial fibrosis (Fig. 4d) and percentage of glomeruli with global glomerulosclerosis (GS; Fig. 4e), a metric commonly used for assessment of donor kidney quality in the United States, correlated poorly with eGFR at 9–12 months post-transplant (PSR: $r = 0.01$, $P = 0.9$; GS: $r = -0.16$, $P = 0.3$). We hypothesized that this result might be due to spatial heterogeneity in fibrosis distribution, meaning that fibrosis levels at the biopsy site may not accurately reflect whole-kidney fibrotic burden. Therefore, we assessed whether fibrosis estimates derived from H-scans performed only at the biopsy site would also correlate less strongly with eGFR post-transplant. As expected, H-scans
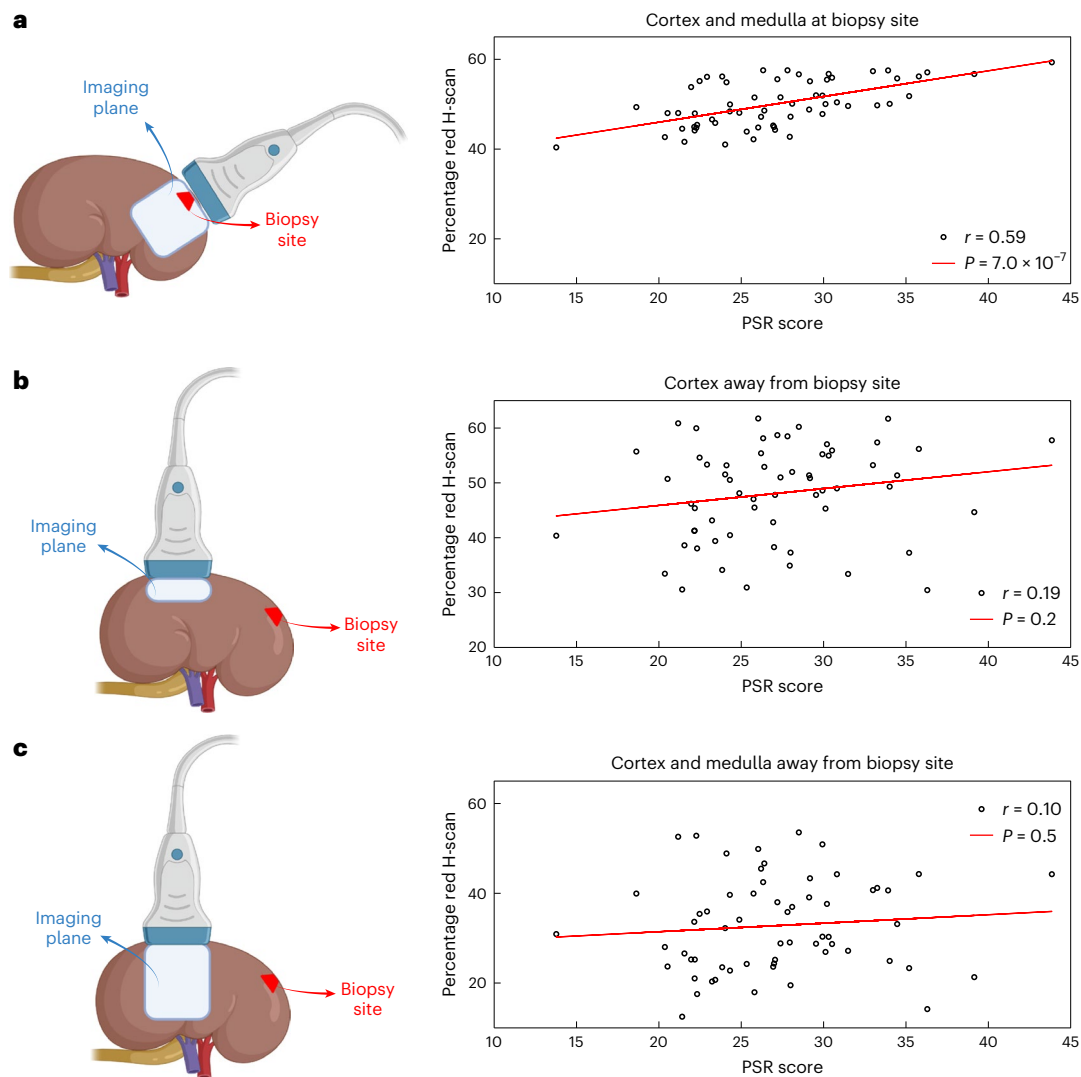
Fig. 3 | H-scan can detect intra-kidney spatial variation in fibrosis. a–c, Imaging plane schematic and correlation of H-scan with PSR for cortex and medulla ROI at the biopsy site (**a**), the cortex away from the biopsy site (**b**) and cortex and medulla away from the biopsy site (**c**). **b,c**, A longitudinal imaging plane was taken through the kidney. Pearson correlation coefficients (*r*) and corresponding *P* values are shown. **a–c** created with BioRender.com.

performed only at the biopsy site (Fig. 4f) also correlated poorly with eGFR at 9–12 months post-surgery (*r* = 0.03, *P* = 0.8). Taken together, our results indicate that whole-kidney H-scan imaging was the only fibrosis measure tested that associated with eGFR at 9–12 months post-transplant, whereas other, more localized, measurements (H-scan at the biopsy site, biopsy-based histologic analyses) did not.

Discussion

Kidney fibrosis is a near-universal feature of chronic kidney disease. Renal fibrotic burden is thus an important biomarker of irreversible injury that correlates negatively with kidney function. Despite its importance, scientists and clinicians currently have no way to non-invasively assess renal fibrotic burden, and thus are forced to rely on either nephrectomy (in the case of experimental rodent models) or biopsy (in the case of humans) for histologic examination. In both cases, this requirement for tissue opens the door to significant sampling bias, because usually only a single, several-microns-thick section of the excised rodent kidney is analyzed, whereas a human kidney biopsy samples <1% of kidney volume. Finally, because biopsy is associated with significant bleeding risk, clinicians choose not to biopsy in many cases and, when they do, as is frequently the case in the assessment of donor kidneys being considered for transplant in the United States, the

resultant findings may not reflect the actual burden of fibrotic damage[11]. Importantly, this inaccuracy probably leads to excessively high discard rates and, thus, fewer kidney transplants in the United States[11]. Here, we describe renal H-scan, an algorithm that can use standard ultrasound data to quickly, easily, accurately and noninvasively quantify whole-kidney fibrotic burden in both mice and humans. Taking advantage of custom-designed, kidney-specific, H-scan algorithms that decode raw RF data generated by ultrasound imaging, we show that renal H-scan strongly correlates with renal fibrotic burden. Importantly, H-scan provides highly reproducible estimates of renal fibrosis that not only identify differences in fibrotic burden between kidneys, but also spatially discrete differences within a given kidney (Extended Data Figs. 1 and 3). We further demonstrate the potential clinical value of this technique, showing that donor kidney fibrotic burden quantified by a pretransplant H-scan is negatively associated with kidney function post-transplant (Fig. 4).

Importantly, renal H-scan software can potentially be added to any standard ultrasound workflow, meaning that widely available conventional ultrasound probes can be used with this algorithm to rapidly and easily estimate whole-kidney fibrotic burden. Unlike other fibrosis imaging strategies, renal H-scan does not require specialized equipment or potentially harmful contrast agents. However, because
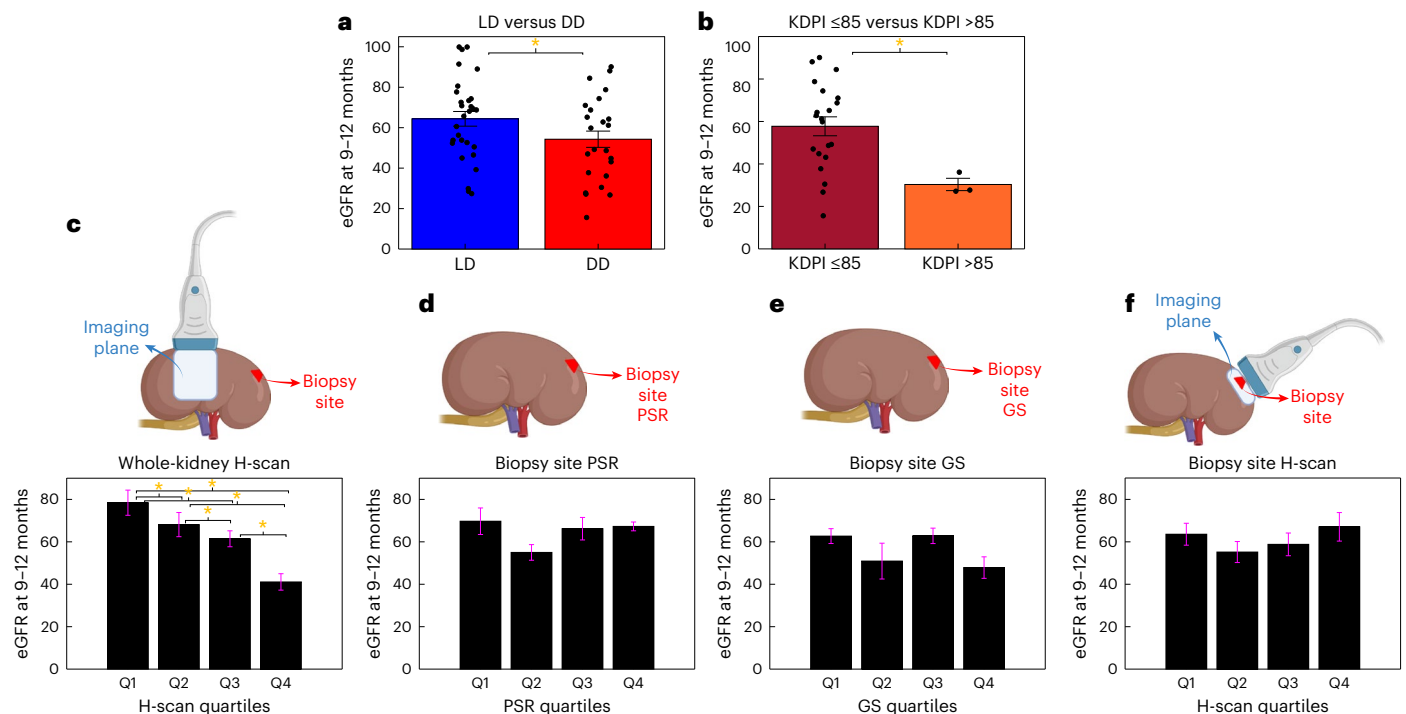
Fig. 4 | Whole kidney H-scan imaging correlates with post-transplant renal function. a, Average eGFR values at 9–12 months post-transplant for LD and DD kidney transplant recipients. **b**, eGFR values at 9–12 months post-transplant for KDPI ≤ 85% and KDPI > 85% kidneys. **c–f**, Mean eGFR values at 9–12 months post-transplant, organized by quartiles (Q1–Q4) of whole-kidney H-scan renal fibrosis measurements (**c**), biopsy site cortex PSR staining (**d**), percentage of glomeruli with global glomerulosclerosis (**e**) and biopsy site cortex H-scan renal fibrosis measurements (**f**). Data presented as mean ± s.e. **a**,**b**, A two-tailed Student's *t*-test was used. An independent samples *t*-test comparison for LD versus DD patient eGFR yielded the following test statistics: $P = 0.0086$, $F = 3.07$, 95% CI [−1.47, 21.64], $\eta = 0.10$; comparison of KDPI yielded the following statistics: $P = 0.033$, $F = 5.15$, 95% CI [2.34, 52.44], $\eta = 0.20$. **c–f**, One-way ANOVA with post hoc Tukey's honestly significant difference analysis was performed, with

Bonferroni-corrected significance and testing for effect size. For whole-kidney H-scan, ANOVA statistical results are: $F_{(3, 52)} = 7.36$, $P = 3.63 \times 10^{-4}$, $\eta = 0.31$, Q1 versus Q2 $P = 0.0070$, Q1 versus Q3 $P = 0.025$, Q1 versus Q4 $P = 0.0016$, Q2 versus Q3 $P = 0.0071$, Q2 versus Q4 $P = 0.0019$, Q3 versus Q4 $P = 0.015$. For biopsy site PSR, ANOVA statistical results are: $F_{(3, 52)} = 1.44$, $P = 0.24$, $\eta = 0.081$, Q1 versus Q2 $P = 0.47$, Q1 versus Q3 $P = 0.99$, Q1 versus Q4 $P = 1.00$, Q2 versus Q3 $P = 0.35$, Q2 versus Q4 $P = 0.85$, Q3 versus Q4 $P = 1.00$. For biopsy site GS, ANOVA statistical results are: $F_{(3, 52)} = 1.15$, $P = 0.34$, $\eta = 0.066$, Q1 versus Q2 $P = 0.49$, Q1 versus Q3 $P = 1.00$, Q1 versus Q4 $P = 0.55$, Q2 versus Q3 $P = 0.75$, Q2 versus Q4 $P = 1.00$, Q3 versus Q4 $P = 0.72$. For biopsy site H-scan, ANOVA statistical results are: $F_{(3, 52)} = 0.71$, $P = 0.55$, $\eta = 0.042$, Q1 versus Q2 $P = 0.73$, Q1 versus Q3 $P = 0.94$, Q1 versus Q4 $P = 0.99$, Q2 versus Q3 $P = 0.96$, Q2 versus Q4 $P = 0.57$, Q3 versus Q4 $P = 0.81$. *$P < 0.05$. **c–f** created with BioRender.com.

it images only the kidney, renal H-scan reports only on kidney fibrosis levels and not on systemic fibrotic burden, which differentiates it from blood-based markers that often reflect fibrosis in all tissues. Thus, renal H-scan software is ideally positioned for rapid translation as a tool for scientists and clinicians to specifically measure whole-kidney fibrotic burden.

Beyond its ability to quantify whole-kidney matrix levels, a key benefit of renal H-scan is its ability to quickly and noninvasively sample tissue across a wide spectrum of length scales, ranging from small areas of interest to the entire kidney (Extended Data Figs. 1 and 3). Thus, renal H-scan can also be used to characterize the heterogeneous spatial distribution of matrix deposition within a given kidney. Importantly, this intrarenal heterogeneity has long been a major limitation of histologic analyses of renal fibrotic burden, given that a biopsy samples <1% of the entire kidney volume and is usually performed only in the cortex. We demonstrate how this spatial heterogeneity can influence the results of biopsy-based histologic analysis, because our H-scan fibrosis measurements correlated tightly with biopsy-based measures only when the H-scan was performed at the same biopsy site. When the H-scan ROI was moved further away from the location of the biopsy, the correlation between biopsy-based histologic fibrosis scores and those generated by H-scan progressively worsened. Although beyond the scope of the current manuscript, it is possible that renal H-scan might be used in the future to better understand how the spatial organization of matrix differs following various types of kidney injury, and over time.

Moreover, fibrosis is usually the consequence of other underlying diseases that, unlike fibrosis, might be amenable to treatment. Because these treatable diseases typically localize to nonscarred areas of the kidney, renal H-scan might also enable biopsy targeting to locations within the kidney that are less scarred, to allow identification of these treatable forms of injury.

Another clinical advantage of renal H-scan is its ability to be performed rapidly without the requirement for specialized expertise. Kidney tissue processing, staining and analysis are time consuming, ranging from hours for frozen sections to days for formalin-fixed, paraffin-embedded tissue, the latter not being possible for donor kidneys given the limited time available for assessment. Histologic fibrosis measurements also ideally require an expert renal pathologist, which adds further time and expertise that is not always available, especially in the context of time-sensitive donor kidney analyses. Automated algorithms for fibrosis quantification of stained tissue sections have been developed, but these generally require whole-slide scanning and, at least currently, are still time intensive and often require human curation. In contrast, a renal H-scan is noninvasive, takes only several minutes and can be performed with a standard US probe, which clinicians often have experience using.

Clinical criteria for assessment of donor kidney quality are well established, with perhaps the most widely used being KDPI. A high KDPI score is thought to correlate with higher levels of chronic damage in the donor kidney although, to date, it has been impossible to correlate

these clinical parameters with a comprehensive histologic analysis because a biopsy samples <1% of the kidney. In contrast, H-scan measurements correlate directly with whole-kidney fibrotic burden, one of the most common and important forms of chronic kidney damage[13,35]. Importantly, fibrosis estimates from a single, longitudinal-axis H-scan performed before transplantation were found to be predictive of kidney function 1 year post-transplant, with higher H-scan-derived fibrosis estimates at the time of transplant correlating with poorer allograft function. Although this preliminary finding will need further validation, because fibrosis is such an important biomarker of chronic renal injury, our results point to H-scan as a potential new tool for assessment of donor kidney quality that could significantly impact decisions regarding kidney acceptance and allocation.

Renal H-scan processes the raw RF data generated by backscattered acoustic waves created during conventional ultrasound scanning. Historically, manufacturers of ultrasound systems have created their own software to convert these RF data into images. Unfortunately, this software differs between manufacturers and can even vary across models from the same company. As a result, although images of the same sample produced by different ultrasound machines can appear macroscopically similar on B-mode, each can vary significantly on a pixel-by-pixel basis. These differences have an important consequence—unlike other modalities, such as computed tomography, conventional ultrasound images cannot be used for quantification because images of the same sample generated by different systems will produce different data. In contrast, H-scan uses raw RF data before conversion to an image and thus, if collected with the same image acquisition settings, will produce similar results regardless of the imaging system used. Moreover, because H-scan is an algorithm that processes RF data and uses this output for fibrosis estimates, and because all ultrasound systems generate these RF data, our algorithm can be readily added to conventional ultrasound machines to add renal fibrosis imaging capability. Finally, unlike other fibrosis imaging tools that have been proposed[21,36–41], renal H-scan uses commonly available equipment (standard ultrasound probes) and does not require the use of exogenous and potentially nephrotoxic agents. Therefore, we envision that this algorithm could be quickly and safely translated for widespread use in both preclinical and clinical settings.

Renal H-scan does not directly measure matrix components, unlike other molecule-specific imaging techniques such as matrix-targeted contrast magnetic resonance imaging[37] or collagen-specific photoacoustic imaging[36]. Instead, it estimates the size of tissue microstructures responsible for the backscattering of ultrasound waves. Although we have shown in the current manuscript that our techniques accurately assess fibrotic burden in the kidney, and the liver in previous work[42], we have not independently confirmed precisely which tissue structures are responsible for this shift towards larger scatterers. However, it is plausible that the deposited matrix may form new, larger structural units that jointly scatter ultrasound waves rather than the smaller base components of the renal vasculature and tubules. Future studies using custom-designed phantoms that better mimic healthy and fibrotic kidney tissues will be required to determine the larger scattering structures detected by H-scan as kidney scars.

A key limitation of the current study is that all H-scan imaging was peformed on ex vivo kidneys. Recognizing that matrix deposition is highly heterogeneous, we took this initial approach to ensure that imaging and histology assessments were performed as close as possible spatially to each other. However, the translational potential of renal H-scan would be augmented if this imaging could be performed in vivo from the skin surface. We have recently shown that in vivo H-scan imaging of the liver, an organ located closer to the skin surface and thus more readily accessible to ultrasound imaging, can accurately assess hepatic fibrotic burden in rodent disease models[32,42]. Ongoing studies in the laboratory are now testing the ability to similarly perform in vivo kidney imaging, not only in rodents but also in humans.

In summary, this study reports an ultrasound-based H-scan technique that measures the fibrotic content of the kidney. We show that renal H-scan is a noninvasive and highly accurate method for measurement of fibrotic burden in experimental mouse models of disease, human nephrectomy specimens and in human donor kidneys before transplant. We further demonstrate that renal H-scan can identify small differences in matrix content between kidney samples and even within parts of the same kidney. Finally, because fibrosis is an important biomarker of chronic renal damage, we show that renal H-scan estimates of donor kidney fibrotic burden inversely correlate with post-transplant kidney function. These results suggest that H-scan may be useful for quantifying renal fibrotic burden in preclinical and human kidney injury models. In the case of human kidney imaging, we also demonstrate the clinical potential of renal H-scan as an innovative method for rapid assessment of donor kidney quality.

Online content

Any methods, additional references, Nature Portfolio reporting summaries, source data, extended data, supplementary information, acknowledgements, peer review information; details of author contributions and competing interests; and statements of data and code availability are available at https://doi.org/10.1038/s41591-024-03417-5.

References

1. Lentine, K. L., Smith, J. M., Millter, J. M. & Bradbrook, K. OPTN/SRTR 2021 Annual Data Report. Kidney. *Organ Procurement and Transplant Network* https://optn.transplant.hrsa.gov/data/view-data-reports/national-data/# (2021).
2. Organ donation statistics. *HRSA* https://www.organdonor.gov/learn/organ-donation-statistics (2024).
3. Stewart, D., Mupfudze, T. & Klassen, D. Does anybody really know what (the kidney median waiting) time is? *Am. J. Transplant.* **23**, 223–231 (2023).
4. Rao, P. S. et al. A comprehensive risk quantification score for deceased donor kidneys: the kidney donor risk index. *Transplantation* **88**, 231–236 (2009).
5. *Kidney Allocation System (KAS) Clarifications & Clean Up* OPTN/UNOS Policy Notice (Kidney Transplant Committee, 2016); https://optn.transplant.hrsa.gov/media/1876/kidney_policynotice_kas_201606.pdf
6. US Department of Health & Human Services. OPTN/SRTR 2018 Annual Data Report: Kidney. *Scientific Registry of Transplant Recipients* http://srtr.transplant.hrsa.gov/annual_reports/Default.aspx (2018).
7. Dahmen, M. et al. Validation of the Kidney Donor Profile Index (KDPI) to assess a deceased donor's kidneys' outcome in a European cohort. *Sci. Rep.* **9**, 11234 (2019).
8. Peters-Sengers, H. et al. Validation of the Prognostic Kidney Donor Risk Index scoring system of deceased donors for renal transplantation in the Netherlands. *Transplantation* **102**, 162–170 (2018).
9. Gupta, A., Francos, G., Frank, A. M., & Shah, A. P. KDPI score is a strong predictor of future graft function: moderate KDPI (35-85) and high KDPI (> 85) grafts yield similar graft function and survival. *Clin. Nephrol.* **86**, 175–182 (2016).
10. Lentine, K. L. et al. Deceased donor procurement biopsy practices, interpretation, and histology-based decision-making: a survey of US kidney transplant centers. *Kidney Int. Rep.* **7**, 1268–1277 (2022).
11. Reese, P. P. et al. Assessment of the utility of kidney histology as a basis for discarding organs in the United States: a comparison of international transplant practices and outcomes. *J. Am. Soc. Nephrol.* **32**, 397–409 (2021).
12. Meng, X.-M., Nikolic-Paterson, D. J. & Lan, H. Y. Inflammatory processes in renal fibrosis. *Nat. Rev. Nephrol.* **10**, 493–503 (2014).

13. De Vusser, K. et al. The predictive value of kidney allograft baseline biopsies for long-term graft survival. *J. Am. Soc. Nephrol.* **24**, 1913–1923 (2013).

14. Watson, C. J. E., Johnson, R. J., Birch, R., Collett, D. & Bradley, J. A. A simplified donor risk index for predicting outcome after deceased donor kidney transplantation. *Transplantation* **93**, 314–318 (2012).

15. Ahmad, I. Biopsy of the transplanted kidney. *Semin. Interv. Radiol.* **21**, 275–281 (2004).

16. Wang, C. J., Wetmore, J. B., Crary, G. S. & Kasiske, B. L. The donor kidney biopsy and its implications in predicting graft outcomes: a systematic review. *Am. J. Transplant.* **15**, 1903–1914 (2015).

17. Whittier, W. L., Gashti, C., Saltzberg, S. & Korbet, S. Comparison of native and transplant kidney biopsies: diagnostic yield and complications. *Clin. Kidney J.* **11**, 616–622 (2018).

18. Kolofousi, C. et al. Ultrasonographic features of kidney transplants and their complications: an imaging review. *ISRN Radiol.* **2013**, 480862 (2013).

19. Rodgers, S. K., Sereni, C. P. & Horrow, M. M. Ultrasonographic evaluation of the renal transplant. *Radiol. Clin. North Am.* **52**, 1307–1324 (2014).

20. Wong, W. et al. Transplant renal artery stenosis in 77 patients– does it have an immunological cause? *Transplantation* **61**, 215–219 (1996).

21. Hysi, E. & Yuen, D. A. Imaging of renal fibrosis. *Curr. Opin. Nephrol. Hypertens.* **29**, 599–607 (2020).

22. Cloutier, G., Destrempes, F., Yu, F. & Tang, A. Quantitative ultrasound imaging of soft biological tissues: a primer for radiologists and medical physicists. *Insights Imaging* **12**, 127 (2021).

23. Lizzi, F. L., Ostromogilsky, M., Feleppa, E. J., Rorke, M. C. & Yaremko, M. M. Relationship of ultrasonic spectral parameters to features of tissue microstructure. *IEEE Trans. Ultrason. Ferroelectr. Freq. Control* **34**, 319–329 (1987).

24. Czarnota, G. J. et al. Ultrasonic biomicroscopy of viable, dead and apoptotic cells. *Ultrasound Med. Biol.* **23**, 961–965 (1997).

25. Kolios, M. C. & Czarnota, G. J. Potential use of ultrasound for the detection of cell changes in cancer treatment. *Future Oncol.* **5**, 1527–1532 (2009).

26. Mamou, J. & Oelze, M. L. *Quantitative Ultrasound in Soft Tissues* (Springer, 2013); https://doi.org/10.1007/978-94-007-6952-6

27. Sadeghi-Naini, A. et al. Quantitative ultrasound spectroscopic imaging for characterization of disease extent in prostate cancer patients. *Transl. Oncol.* **8**, 25–34 (2015).

28. Oelze, M. L. & Mamou, J. Review of quantitative ultrasound: envelope statistics and backscatter coefficient imaging and contributions to diagnostic ultrasound. *IEEE Trans. Ultrason. Ferroelectr. Freq. Control* **63**, 336–351 (2016).

29. Parker, K. J. Scattering and reflection identification in H-scan images. *Phys. Med. Biol.* **61**, L20–L28 (2016).

30. Khairalseed, M., Hoyt, K., Ormachea, J., Terrazas, A. & Parker, K. J. H-scan sensitivity to scattering size. *J. Med. Imaging (Bellingham)* **4**, 043501 (2017).

31. Parker, K. J. & Baek, J. Fine-tuning the H-scan for discriminating changes in tissue scatterers. *Biomed. Phys. Eng. Express* **6**, 045012 (2020).

32. Baek, J., Basavarajappa, L., Hoyt, K. & Parker, K. J. Disease-specific imaging utilizing support vector machine classification of H-scan parameters: assessment of steatosis in a rat model. *IEEE Trans. Ultrason. Ferroelectr. Freq. Control* **69**, 720–731 (2022).

33. Bülow, R. D. & Boor, P. Extracellular matrix in kidney fibrosis: more than just a scaffold. *J. Histochem. Cytochem.* **67**, 643–661 (2019).

34. Farris, A. B. & Alpers, C. E. What is the best way to measure renal fibrosis?: a pathologist's perspective. *Kidney Int. Suppl.* **4**, 9–15 (2014).

35. Srivastava, A. et al. The prognostic value of histopathologic lesions in native kidney biopsy specimens: results from the Boston Kidney Biopsy Cohort Study. *J. Am. Soc. Nephrol.* **29**, 2213–2224 (2018).

36. Hysi, E. et al. Photoacoustic imaging of kidney fibrosis for assessing pretransplant organ quality. *JCI Insight* **5**, e136995 (2020).

37. Sun, Q. et al. Elastin imaging enables noninvasive staging and treatment monitoring of kidney fibrosis. *Sci. Transl. Med.* **11**, eaat4865 (2019).

38. Samir, A. E. et al. Shear wave elastography in chronic kidney disease: a pilot experience in native kidneys. *BMC Nephrol.* **16**, 119 (2015).

39. Leung, G. et al. Could MRI be used to image kidney fibrosis? A review of recent advances and remaining barriers. *Clin. J. Am. Soc. Nephrol.* **12**, 1019–1028 (2017).

40. Berchtold, L. et al. Validation of the corticomedullary difference in magnetic resonance imaging-derived apparent diffusion coefficient for kidney fibrosis detection: a cross-sectional study. *Nephrol. Dial. Transplant.* **35**, 937–945 (2019).

41. Friedli, I. et al. New magnetic resonance imaging index for renal fibrosis assessment: a comparison between diffusion-weighted imaging and T1 mapping with histological validation. *Sci. Rep.* **6**, 30088 (2016).

42. Baek, J., Poul, S. S., Swanson, T. A., Tuthill, T. & Parker, K. J. Scattering signatures of normal versus abnormal livers with support vector machine classification. *Ultrasound Med. Biol.* **46**, 3379–3392 (2020).

¹Department of Medical Biophysics, Temerty Faculty of Medicine, University of Toronto, Toronto, Ontario, Canada. ²Keenan Research Centre for Biomedical Science, Li Ka Shing Knowledge Institute, St. Michael's Hospital, Unity Health Toronto, Toronto, Ontario, Canada. ³Institute for Biomedical Engineering, Science and Technology (iBEST), A partnership between Toronto Metropolitan University and St. Michael's Hospital, Toronto, Ontario, Canada. ⁴Department of Physics, Faculty of Science, Toronto Metropolitan University, Toronto, Ontario, Canada. ⁵Department of Electrical and Computer Engineering, University of Rochester, Rochester, NY, USA. ⁶Division of Urology, Department of Surgery, St. Michael's Hospital, Unity Health Toronto and University of Toronto, Toronto, Ontario, Canada. ⁷Division of Nephrology, Department of Medicine, St. Michael's Hospital, Unity Health Toronto and University of Toronto, Toronto, Ontario, Canada. ⁸Department of Laboratory Medicine, St. Michael's Hospital, Unity Health Toronto and University of Toronto, Toronto, Ontario, Canada. ⁹These authors contributed equally: Jihye Baek, Alexander Koven. ¹⁰These authors jointly supervised this work: Michael C. Kolios, Kevin J. Parker, Darren A. Yuen. ✉e-mail: darren.yuen@utoronto.ca

Methods

Unilateral ureteral obstruction model of kidney fibrosis

Kidneys from a previously published group of 6–8-week-old male C57BL/6 mice (Charles River Laboratories) that had undergone left-sided UUO surgery were studied[36]. Mice were housed under a 12/12-h light/dark cycle, a temperature of 21 °C and humidity 30–50%. Briefly, the left kidney and ureter were identified through a left-sided flank incision created in anesthetized mice. To induce fibrosis, the left ureter of $n = 10$ mice was obstructed using surgical sutures, just distal to the renal pelvis, resulting in impaired urinary obstruction and progressive fibrosis. The contralateral right kidney was not injured and served as a healthy, nonfibrotic control. In addition, $n = 5$ mice (sham) also served as controls, in which a similar flank incision was made without obstructing the ureter[36]. Sham-operated animals ($n = 5$) were followed for 14 days post-surgery, whereas UUO mice were sacrificed on day 7 ($n = 5$) and day 14 ($n = 5$) post-surgery. For all mice ($n = 15$), the left and right kidneys were extracted and each kidney was imaged before histologic analysis.

Human nephrectomy specimens

Residual kidney tissue from clinically indicated radical nephrectomy surgeries performed for renal cancer was collected at St. Michael's Hospital as part of a previously published study ($n = 5$ patients)[36]. A portion of the renal cortex and medulla was collected from the noncancerous pole of the excised kidneys and submerged in 4 °C PBS until ultrasound imaging was performed.

Preclinical kidney and nephrectomy specimen imaging

Imaging was performed using a VevoLAZR-X imaging system with a 15 MHz, center-frequency, linear-array probe containing 256 elements (FujiFilm-VisualSonics, Inc.)[43]. For mouse kidney imaging, each kidney was excised and placed in a container with PBS maintained at 4 °C, and two-dimensional B-mode ultrasound images were acquired through the longest longitudinal cross-section of the kidney. A total of 59 temporal acquisitions were acquired at an imaging frame rate of 5 Hz. Imaging of human nephrectomy specimens (Fig. 1a) was performed by mounting the probe onto a three-dimensional motor capable of scanning at a step size of 150 μm, which is well below the elevational resolution of the imaging system. A total of 130 two-dimensional scans were acquired, covering the entire length of the specimens at an imaging frame rate of 5 Hz.

Design of clinical study

We performed a first-in-human prospective cohort study at St. Michael's Hospital between December 2021 and May 2023. All patients undergoing kidney transplantation were eligible for the study. The only exclusion criterion was lack of informed consent. The following information was collected from enrolled kidney transplant recipients: age, self-reported gender, height, weight, initial cause of end-stage kidney disease, type of dialysis, dialysis vintage and immunosuppression regimen (induction and maintenance). We also recorded cold and warm ischemia times for each kidney. The following demographic and clinical characteristics were collected from kidney donors: age, self-reported gender, height, weight, ethnicity, history of hypertension, history of diabetes, donor type (neurological determination of death, NDD versus DCD), cause of death and terminal serum creatinine and CKD-EPI 2021, eGFR and hepatitis C serology). The KDPI was calculated from the above data[4]. All data were stored in REDCap (v.14.0.44, Vanderbilt University, Nashville, TN).

Human transplant kidney imaging protocol

Following fat removal and kidney inspection, a small wedge biopsy was performed at the upper pole of each donor kidney (Fig. 2a). Each kidney then underwent sterile, blood-free ultrasound imaging on the back table (5 min duration) while the recipient was being prepared for surgery (thus not extending cold ischemia time). Kidneys were maintained

on ice-cold slush during imaging, and sterile ultrasound gel was used to couple the probe with the kidney. Imaging was performed on either side of the kidney along two planes: (1) the longest longitudinal plane of the kidne (scan nos. 1 and 3) and (2) transversely at the biopsy site (scan nos. 2 and 4) (Fig. 2a).

Development of a renal H-scan algorithm

Extended Data Fig. 3 provides a schematic illustrating the stepwise development of the renal H-scan algorithm. H-scan relies on quantifying the spectral shifts of reflected echoes from ultrasonic scatterers, using matched filters to extract differences in scatterer size[29,31]. To extract such spectral shifts, which we hypothesized would change as renal fibrosis developed, Gaussian functions were first generated and subsequently convolved with the backscattered ultrasound data. To remove depth- and frequency-dependent attenuation effects on scatterer size estimations, each ROI was divided into ten ROI attenuation zones. Extended Data Fig. 3a shows representative raw and attenuation-corrected RF data. Attenuation correction was performed by multiplying the spectrum of each of the ten ROI zones by $e^{+\alpha f x_z}$ (α is the attenuation coefficient, f is a transmit frequency of a transducer and x^z is a representative depth for the zth area index). For mouse kidneys and human nephrectomy specimens, the attenuation coefficient chosen was 0.5 dB cm^{-1} MHz and was assumed to be uniform throughout the entire kidney. This coefficient was further adjusted to account for the reduced imaging temperature of human transplanted whole kidneys, because these were imaged at 4 °C. The axial profile of the dominant frequency contained within the RF signal reveals the effect of attenuation correction in the plot shown in Extended Data Fig. 3a.

The resulting attenuation-corrected RF backscattered data were then used as input for the H-scan algorithm. A total of 256 Gaussian-matched filters were created based on the center frequency and bandwidth of the 15-MHz transmit center-frequency transducer used in this study, as illustrated in Extended Data Fig. 3b. Specifically, filter G_1 had a center frequency 70% lower than that of the measured spectrum and a 70% bandwidth. The center frequency of the subsequent matched filters (G_2–G_{256}) was increased proportionally, up to 70% higher than that of the measured power spectrum. Using each of the matched Gaussian functions as a band-pass filter, the frequency spectrum of attenuation-corrected RF data was filtered for each scanline at each attenuation zone. Inverse Fourier transform converted the data back into the time domain. This is also the equivalent of a convolution of 256 band-passed filtered RF signals in the temporal domain.

As illustrated in Extended Data Fig. 3c, this operation resulted in 256 normalized convolution values (band-passed filter output amplitudes). The maximum value of this convolution was then identified, enabling assignment of the corresponding Gaussian filtered index for a given RF line (shown on the x axis). Because each of the 256 Gaussian filters has a unique peak frequency, the corresponding peak frequency can then be assigned to each depth in the sample. H-scan color mapping was then performed by matching the 256 frequencies to 256 color levels, from red (color level 1) to blue (color level 256). As such, color levels 1–128 correspond to lower-frequency components (or larger scatterers) and are pseudo-colorized in various shades of red. Conversely, colors 129–256 correspond to higher-frequency components (or smaller scatterers), which are denoted by blue colors. The center frequency of G_{128} was optimized according to the specific target organ and disease under study. For instance, we have demonstrated in murine liver fibrosis studies that fibrosis with lower steatosis contained more blue colors, while red was more prevalent during fibrosis with higher fat content[42]. By setting the mean of the healthy control kidneys to approximately 50% blue and to the 128-color level, we could visualize various scatterer sizes throughout the kidney.

Extended Data Fig. 3d shows a representative H-scan image from two reference phantoms of different size, chosen to reflect the expected scatterer sizes in the kidney. Both phantoms consisted of

glass beads embedded in a homogenous background of microscopic oil droplets in gelatin[44–46]. The large-scatterer phantom contained beads of average diameter 49.35 ± 10.8 μm; its speed of sound and attenuation at 10 MHz were 1,488 m s^{-1} and 0.719 dB cm^{-1}, respectively. The beads of the small-scatterer phantom had an average diameter of 6.15 ± 1.3 μm, a sound speed of 1,541 m s^{-1} and an attenuation of 0.439 dB cm^{-1} at 10 MHz. Each phantom was scanned with linear-array probes at 15 MHz transmit center frequency, using the 256-element, linear-array part of the VevoLAZR-X system. The probe had spatial resolution of 100 μm, 200 μm and 1.2 mm in the axial, lateral and elevation planes, respectively.

Image preprocessing

Extended Data Fig. 4 shows a schematic depicting how our H-scan technique was adapted for mouse kidney imaging. The kidney was manually contoured before implementing the H-scan algorithm on the whole organ (Extended Data Fig. 4a). Ureteral obstruction causes gross dilation of the renal pelvis and medullary calyces, leading to inner hypoechoic areas within the kidney. These areas were excluded from H-scan analysis through morphological opening (Extended Data Fig. 4b), implemented using built-in Matlab functions (Mathworks v.2021a). Morphological erosion was then used to separate the kidney's outer (cortical) regions from the inner (medullary) regions with erosion Matlab built-in functions. The ratio between the distance from the kidney center to the inner region boundary, and the distance from the inner to outer region boundary, were set to 1. Both the outer and inner regions of the mouse kidney were analyzed, denoting primarily the cortex and medulla, respectively. The morphological opening algorithm was also implemented on human kidney specimens, to exclude hypoechoic or low signal-to-noise regions. However, no separation of the cortex and medulla was performed on human nephrectomy samples because, in most specimens, only the cortex was sampled. For all kidneys, the percentage of red or blue pixels was defined as the ratio between the number of pixels with color range 1–128 (corresponding to red) or 129–256 (corresponding to blue) and the total number of pixels within an ROI. A histogram distribution of H-scan color levels was also generated, to quantify changes in scatterer size for different regions within mouse kidneys or various levels of fibrosis in human kidneys.

Adaptation of renal H-scan to transplanted kidneys

Immediately following donor nephrectomy, the transplant kidney was placed in a crushed-ice solution maintained at 4 °C. The length of time the kidney is kept in this solution (until ready to be transplanted) is referred to as cold ischemia time. Because ultrasound imaging was performed with the kidney in this solution while the recipient was being prepared for surgery, cold ischemic time was not affected by imaging. Ultrasound attenuation is also known to be temperature dependent[47], and the H-scan algorithm developed for mouse kidney was modified to account for this effect by first estimating the attenuation coefficient at 4 °C before correcting the ultrasound backscattered data. Such estimations were compared with known attenuation coefficients for the kidney at physiological temperatures (1.0 dB MHz^{-1} cm^{-1} at 37 °C; ref. 48). Extended Data Fig. 5a shows a schematic of the algorithm used for estimation of the attenuation coefficient from kidney images acquired during this 4 °C imaging. The backscattered ultrasound frequency spectrum can be modeled using the Gaussian function $e^{-\frac{(f-f_0)^2}{2\sigma^2}}$ (f is frequency, f_0 is center frequency for transmission and σ is bandwidth). The attenuation-corrected power spectrum $S(f)$ can be then described by equation (1):

$$S(f) = e^{-\frac{(f-f_0)^2}{2\sigma^2}} \times e^{-\alpha f x} \tag{1}$$

where σ is the attenuation coefficient and x is depth. This peak of this frequency spectrum can be identified by computing when the first

partial derivative of $S(f)$, with respect to frequency f at peak frequency f_p, becomes 0, as shown in equation (2):

$$\left.\frac{\partial S}{\partial f}\right|_{f=f_p} = \left(-\frac{f_p - f_0}{\sigma^2} + \alpha x\right) \times S(f_p) = 0. \tag{2}$$

Because the first term is 0, we obtain equation (3):

$$\frac{f_p - f_0}{\sigma^2} + \alpha x = 0. \tag{3}$$

The solution of this equation can be obtained by taking the first derivative of both sides with respect to x, rewriting the equation as equation (4):

$$\frac{df_p}{dx} = -\alpha\sigma^2. \tag{4}$$

Because the same ultrasound transmission was used regardless of temperature, bandwidth σ for the transmit pulse before attenuation is the same across all temperatures. We can thus rewrite equation (4) as equation (5):

$$\frac{1}{\alpha(T = 4\ °C)}\left.\frac{df_p}{dx}\right|_{T=4\ °C} = \frac{1}{\alpha(T = 37\ °C)}\left.\frac{df_p}{dx}\right|_{T=37\ °C}. \tag{5}$$

To calculate df_p/dx for 4 and 37 °C, peak frequencies along with depth were investigated using H-scan analysis through the first four attenuation blocks in Extended Data Fig. 3. The frequency measures shown in Extended Data Fig. 5b generated the slopes of $\left.\frac{df_p}{dx}\right|_{T=4\ °C} = -2.44$ and $\left.\frac{df_p}{dx}\right|_{T=37\ °C} = -1.45$, when frequency measurement plots were averaged using all enrolled kidneys. Because attenuation at 37 °C is known to be 1.0 dB MHz^{-1} cm^{-1}, the attenuation coefficient at 4 °C was estimated to be 1.7 dB MHz^{-1} cm^{-1} using equation (5) and the measured slopes calculated in Extended Data Fig. 5b. This attenuation value was used to perform the attenuation compensation described in the generic H-scan methodology section summarized in Extended Data Fig. 3.

Tissue collection and histologic quantification of fibrosis

Immediately following ultrasound imaging, each kidney sample or biopsy was immersed in 10% neutral buffered formalin for immediate fixation. Formalin-fixed tissues were embedded in paraffin and sectioned. As shown in Extended Data Fig. 1a, mouse kidneys were sectioned into approximate thirds, at each kidney pole and near the center. Three sections per mouse kidney sample and one per human kidney sample were then stained with PSR (Millipore Sigma), HPS and/ or Masson trichrome to visualize fibrotic matrix. Mouse kidney sections were also stained with antibodies directed against either α-SMA (1:200 dilution, catalog no. M0851, Agilent Dako) or type 1 collagen (1:200, catalog no. 1310-01, Southern Biotech)[36]. Between four and six random, nonoverlapping whole-kidney images (for mouse kidneys) and cortex images (for human kidneys) were collected at ×20 magnification by a blinded observer using an Olympus microscope. Using either Aperio Imagescope (Leica Biosystems) or Halo imaging software (Indica Labs), fibrotic burden was then quantified in a blinded fashion by calculating the ratio of positively stained pixels to total pixels, as previously performed[36,49–52].

Statistics

Unless otherwise noted, data are presented as mean ± s.e. One-way analysis of variance (ANOVA) with post hoc Tukey's analysis was used to investigate differences in H-scan and histological measurements of kidney fibrosis (in both mouse and human samples), as well as clinical measures of kidney function (human samples). To determine the association of fibrosis measurements with eGFR at 9–12 months

post-transplant, we divided the following imaging- and histology-based fibrosis parameters into the following quartiles (Q1–Q4): H-scan whole-kidney ROI: Q1 ≤ 38.70, 38.70 < Q2 ≤ 46.89, 46.89 < Q3 ≤ 55.08, Q4 > 55.08; PSR: Q1 ≤ 21.29, 21.29 < Q2 ≤ 28.81, 28.81 < Q3 ≤ 36.33, Q4 > 36.33; GS: Q1 ≤ 11.77, 11.77 < Q2 ≤ 23.54, 23.54 < Q3 ≤ 35.31, Q4 > 35.31; H-scan subcortical kidney ROI: Q1 ≤ 29.20, 29.20 < Q2 ≤ 35.42, 35.42 < Q3 ≤ 41.64, Q4 > 41.64. An unpaired (independent), two-tailed t-test with 95% CI was used to test statistical significance for pairwise comparisons. Pearson linear correlation coefficients were calculated to evaluate H-scan performance, by comparison with gold standard histology measures and/or clinical measures of kidney function (eGFR). A variable with $P < 0.05$ was considered statistically significant, with Bonferroni correction applied for correlation analyses involving multiple comparisons. All statistical analyses were performed with either Matlab (Mathworks v.2021a) or R language for statistical computing (v.4.1.1, R Core Team).

Ethics approval

All mouse studies were approved by the St. Michael's Hospital Animal Care Committee (Toronto, Canada) and conformed to the Canadian Council on Animal Care guidelines. The Unity Health Toronto Research Ethics Board approved the human protocols used for these experiments (nos. 20-049 and 18-193), which adhered to the Declaration of Helsinki. All patients included within the study provided written informed consent. The clinical and research activities being reported are consistent with the Principles of the Declaration of Istanbul as outlined in the 'Declaration of Istanbul on Organ Trafficking and Transplant Tourism'.

Reporting summary

Further information on research design is available in the Nature Portfolio Reporting Summary linked to this article.

Data availability

All data are presented in the manuscript or in Supplementary Information. For our clinical trial, individual deidentified data that support the findings in this study are not openly available due to privacy requirements imposed by our Research Ethics Board, but are available from the corresponding author on reasonable request. Data are located in controlled access data storage at St. Michael's Hospital.

Code availability

The code used for the H-scan algorithm is available at the following link: https://github.com/University-of-Rochester-URVentures/HScanGUI.

References

43. Needles, A. et al. Development and initial application of a fully integrated photoacoustic micro-ultrasound system. *IEEE Trans. Ultrason. Ferroelectr. Freq. Control* **60**, 888–897 (2013).
44. Madsen, E. L., Hobson, M. A., Shi, H., Varghese, T. & Frank, G. R. Tissue-mimicking agar/gelatin materials for use in heterogeneous elastography phantoms. *Phys. Med. Biol.* **50**, 5597–5618 (2005).
45. Madsen, E. L., Deaner, M. E. & Mehi, J. Properties of phantom tissuelike polymethylpentene in the frequency range 20–70 MHZ. *Ultrasound Med. Biol.* **37**, 1327–1339 (2011).
46. Wirtzfeld, L. A. et al. Cross-imaging platform comparison of ultrasonic backscatter coefficient measurements of live rat tumors. *J. Ultrasound Med.* **29**, 1117–1123 (2010).
47. Thanh, P. V. et al. Effect of temperature on ultrasonic velocities, attenuations, reflection and transmission coefficients between motor oil and carbon steel estimated by pulse-echo technique of ultrasonic testing method. *VNU J. Sci: Math. - Phys* **31**, 39–48 (2015).
48. Shankar, H., Pagel, P. S. & Warner, D. S. Potential adverse ultrasound-related biological effects. *Anesthesiology* **115**, 1109–1124 (2011).
49. Szeto, S. G. et al. YAP/TAZ are mechanoregulators of TGF-β-Smad signaling and renal fibrogenesis. *J. Am. Soc. Nephrol.* **27**, 3117–3128 (2016).
50. Zhang, T. et al. NUAK1 promotes organ fibrosis via YAP and TGF-β/SMAD signaling. *Sci. Transl. Med.* **14**, eaaz4028 (2022).
51. He, X. et al. Myofibroblast YAP/TAZ activation is a key step in organ fibrogenesis. *JCI Insight* **7**, e146243 (2022).
52. Yuen, D. A. et al. Recombinant N-terminal Slit2 inhibits TGF-β-induced fibroblast activation and renal fibrosis. *J. Am. Soc. Nephrol.* **27**, 2609–2615 (2016).

Author contributions

E.H. performed experiments and data analysis and cowrote the manuscript. J.B. developed the H-scan algorithms, performed experiments and analyzed data. X.H. performed experiments and analyzed data. L.U.S. and Y.W. analyzed data. A. Koven, M.F., M.O., K.-H.F., R.S. and K.T.P. performed ultrasound imaging of transplant kidneys. A. Krizova reviewed kidney histology. K.K. and S.H. maintained research databases and performed data analysis. M.C.K. acquired funding, coordinated overall study design and edited the manuscript. K.J.P. developed the H-scan algorithm. D.A.Y. acquired funding, coordinated overall study design and wrote and edited the manuscript.

Competing interests

E.H., J.B., M.C.K., K.J.P. and D.A.Y. declare that they have filed a provisional patent (US 63/598,598) related to this work. The other authors declare no competing interests.

Additional information

Extended data is available for this paper at https://doi.org/10.1038/s41591-024-03417-5.

Supplementary information The online version contains supplementary material available at https://doi.org/10.1038/s41591-024-03417-5.

Correspondence and requests for materials should be addressed to Darren A. Yuen.

Peer review information *Nature Medicine* thanks Deborah Adey and the other, anonymous, reviewer(s) for their contribution to the peer review of this work. Primary Handling Editor: Liam Messin, in collaboration with the *Nature Medicine* team.

Reprints and permissions information is available at www.nature.com/reprints.
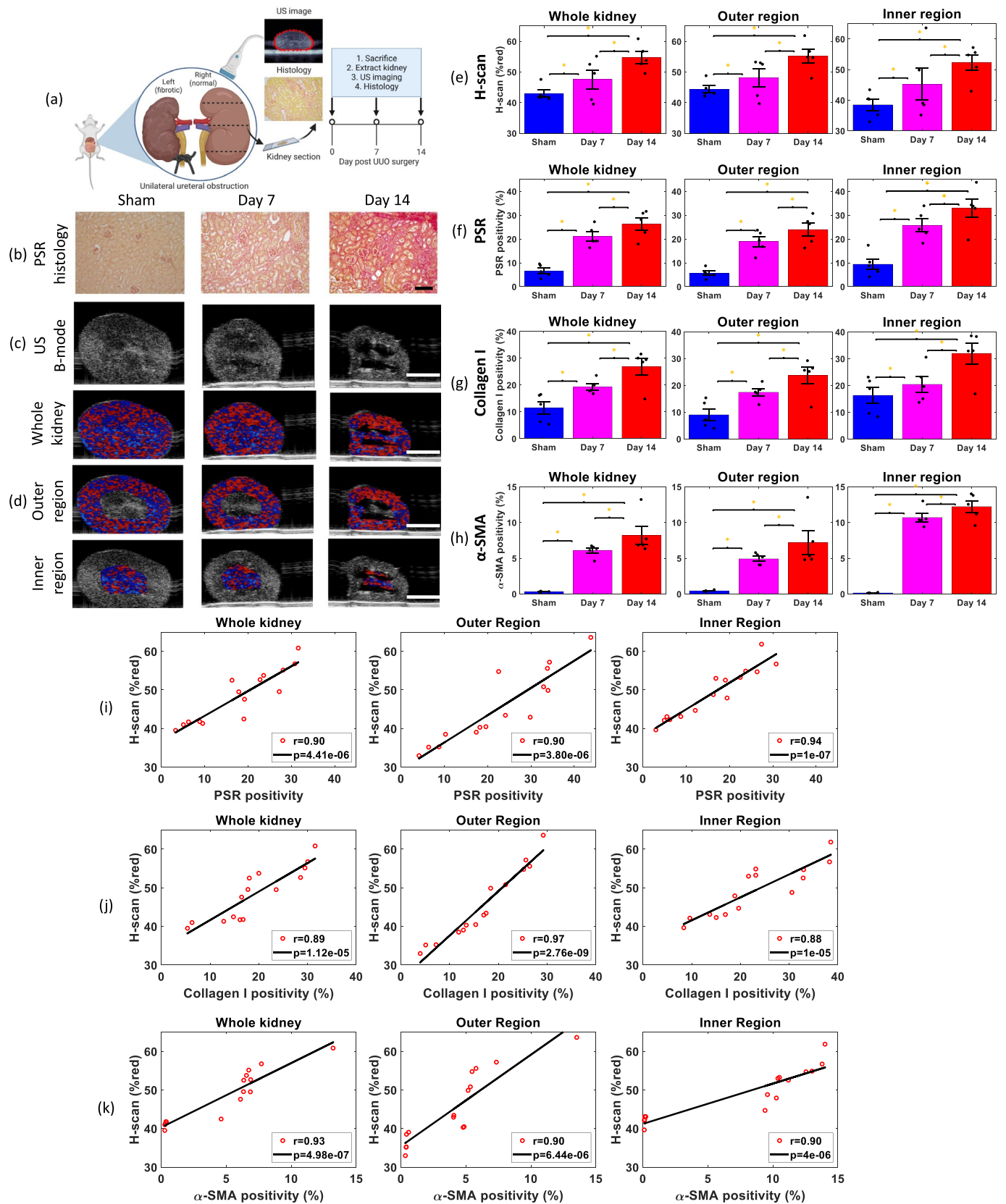
Extended Data Fig. 1 | See next page for caption.

Extended Data Fig. 1 | Renal H-scan accurately tracks the development of mouse kidney fibrosis. (a) Schematic of mouse kidney imaging experiments. **(b)** Representative images of PSR-stained sections from sham kidneys as well as fibrotic kidneys on day 7 and day 14 following UUO surgery. Black scale bar: 100 μm. **(c)** Representative B-mode and **(d)** H-scan images of sham kidneys and kidneys at days 7 and 14 after UUO surgery. The H-scan maps are shown for the whole kidney and the outer (cortex) and inner regions (medulla). White scale bar: 2 mm. **(e)** H-scan-based fibrosis estimates (% red pixel density) of whole kidney, outer kidney, and inner kidney regions based on images of left kidneys of sham mice and day 7 and day 14 post-UUO mice (n = 5/group). For the whole kidney region of interest, a one-way ANOVA revealed a statistically significant difference between the groups $F_{(2, 14)} = 7.11$, $p = 0.0092$, with a large effect size $\eta = 0.54$. Post-hoc analyses with Tukey's Honestly Significant Difference analysis, with Bonferroni-corrected significance revealed a significance difference in H-scan %red between Sham vs. Day 7 ($p = 0.034$), Day 7 vs. Day 14 ($p = 0.097$), and Sham vs. Day 14 ($p = 0.0073$). The same analysis and reporting was performed for the outer and inner kidney regions of interest. For the outer kidney region of interest, the H-scan ANOVA statistical results are: $F_{(2, 14)} = 6.00$, $p = 0.016$, $\eta = 0.50$, Sham vs. Day 7 $p = 0.038$, Day 7 vs. Day 14 $p = 0.011$, Sham vs. Day 14 $p = 0.013$. For the inner kidney region of interest, the H-scan ANOVA statistical results are: $F_{(2, 14)} = 3.81$, $p = 0.042$, $\eta = 0.39$, Sham vs. Day 7 $p = 0.039$, Day 7 vs. Day 14 $p = 0.037$, Sham vs. Day 14 $p = 0.042$. Fibrotic burden measurements using gold standard **(f)** PSR, **(g)** type I collagen, and **(h)** α-SMA stains. For PSR staining, the ANOVA statistical results are: Whole kidney: $F_{(2, 14)} = 26.21$, $p = 4.18$e-5, $\eta = 0.81$, Sham vs. Day 7 $p = 0.0070$, Day 7 vs. Day 14 $p = 0.020$, Sham vs. Day 14 $p = 4.05$e-5; Outer kidney: $F_{(2, 14)} = 21.24$, $p = 1.14$e-, $\eta = 0.78$, Sham vs. Day 7 $p = 0.0017$, Day 7 vs. Day 14 $p = 0.023$, Sham vs. Day 14 $p = 0.00010$; Inner kidney: $F_{(2, 14)} = 15.71$, $p = 4.46$e-4, $\eta = 0.72$, Sham vs. Day 7 $p = 0.0066$, Day 7 vs. Day 14 $p = 0.026$, Sham vs. Day 14 $p = 0.0004$. For type I collagen staining, the ANOVA statistical results are: Whole kidney: $F_{(2, 14)} = 10.92$, $p = 0.0020$, $\eta = 0.54$, Sham vs. Day 7 $p = 0.0085$, Day 7 vs. Day 14 $p = 0.0093$, Sham vs. Day 14 $p = 0.0014$; Outer kidney: $F_{(2, 14)} = 9.95$, $p = 0.0028$, $\eta = 0.62$, Sham vs. Day 7 $p = 0.0061$, Day 7 vs. Day 14 $p = 0.019$, Sham vs. Day 14 $p = 0.0021$; Inner kidney: $F_{(2, 14)} = 5.71$, $p = 0.018$, $\eta = 0.49$, Sham vs. Day 7 $p = 0.0068$, Day 7 vs. Day 14 $p = 0.0079$, Sham vs. Day 14 $p = 0.017$. For α-SMA staining, the ANOVA statistical results are: Whole kidney: $F_{(2, 14)} = 28.10$, $p = 2.97$e-5, $\eta = 0.82$, Sham vs. Day 7 $p = 0.00050$, Day 7 vs. Day 14 $p = 0.016$, Sham vs. Day 14 $p = 2.81$e-5; Outer kidney: $F_{(2, 14)} = 12.29$, $p = 0.0012$, $\eta = 0.67$, Sham vs. Day 7 $p = 0.018$, Day 7 vs. Day 14 $p = 0.0286$, Sham vs. Day 14 $p = 0.0010$; Inner kidney: $F_{(2, 14)} = 122.99$, $p = 1.01$e-8, $\eta = 0.95$, Sham vs. Day 7 $p = 7.87$e-8, Day 7 vs. Day 14 $p = 0.021$, Sham vs. Day 14 $p = 1.72$e-8. Correlation between H-scan based % red pixel density and histologic fibrosis scores derived from **(i)** PSR, **(j)** type I collagen, and **(k)** α-SMA staining for the whole kidney, outer and inner regions. Pearson correlation coefficients (r) and corresponding p values are provided for each comparison in each graph, all of which are statistically significant. Data are presented as mean +/− standard error. * $p < 0.05$. **a** created with BioRender.com.
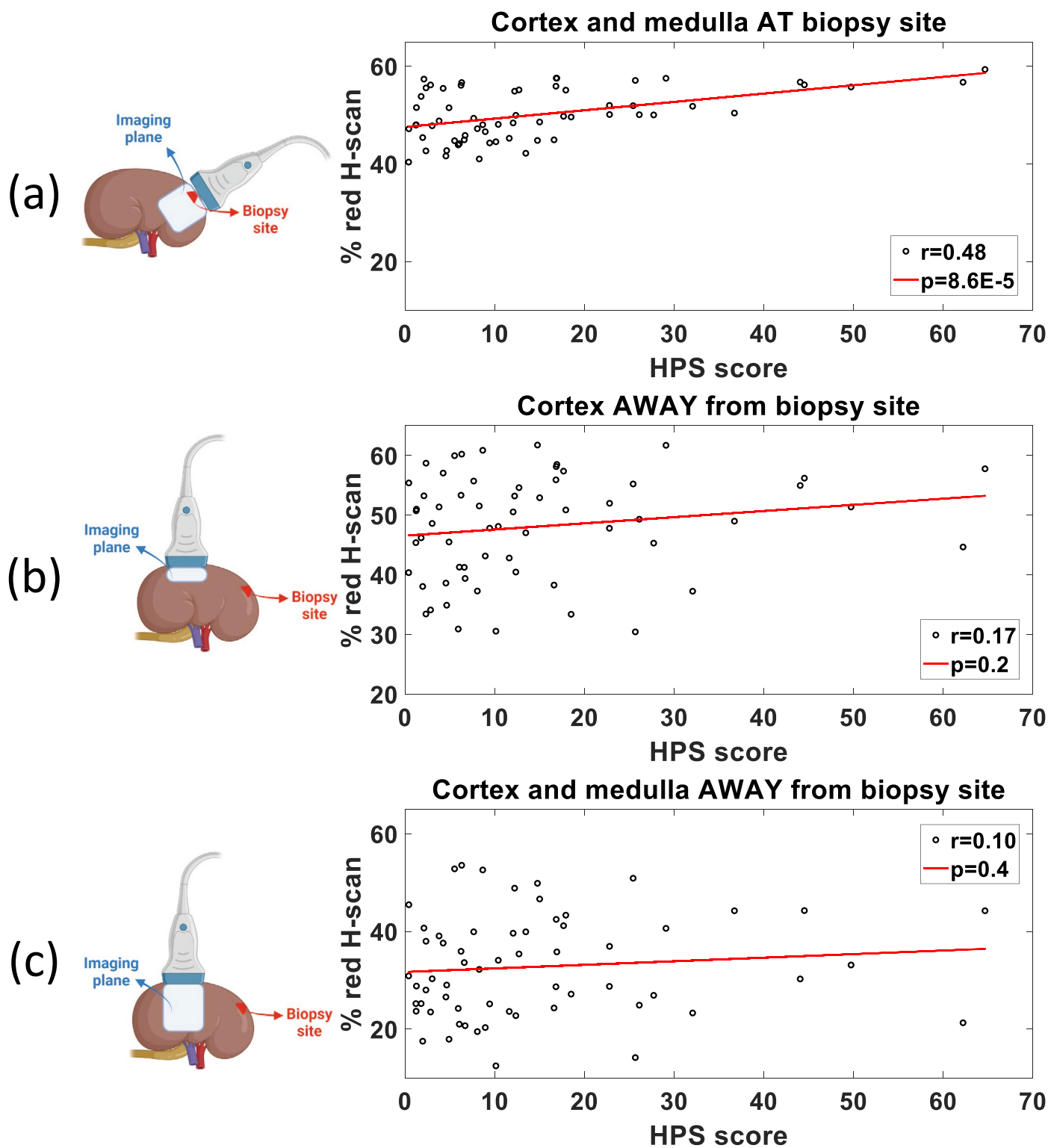
Extended Data Fig. 2 | Spatial heterogeneity of fibrosis distribution as assessed by HPS. Correlations of the H-scan estimates with HPS for ROI drawn in (**a**) the cortex and medulla at the biopsy site, (**b**) the cortex away from the biopsy site, and (**c**) the cortex and medulla away from the biopsy site. Pearson correlation coefficients (*r*) and corresponding *p* values are provided for each comparison in each graph, none of which are statistically significant. Created with BioRender.com.
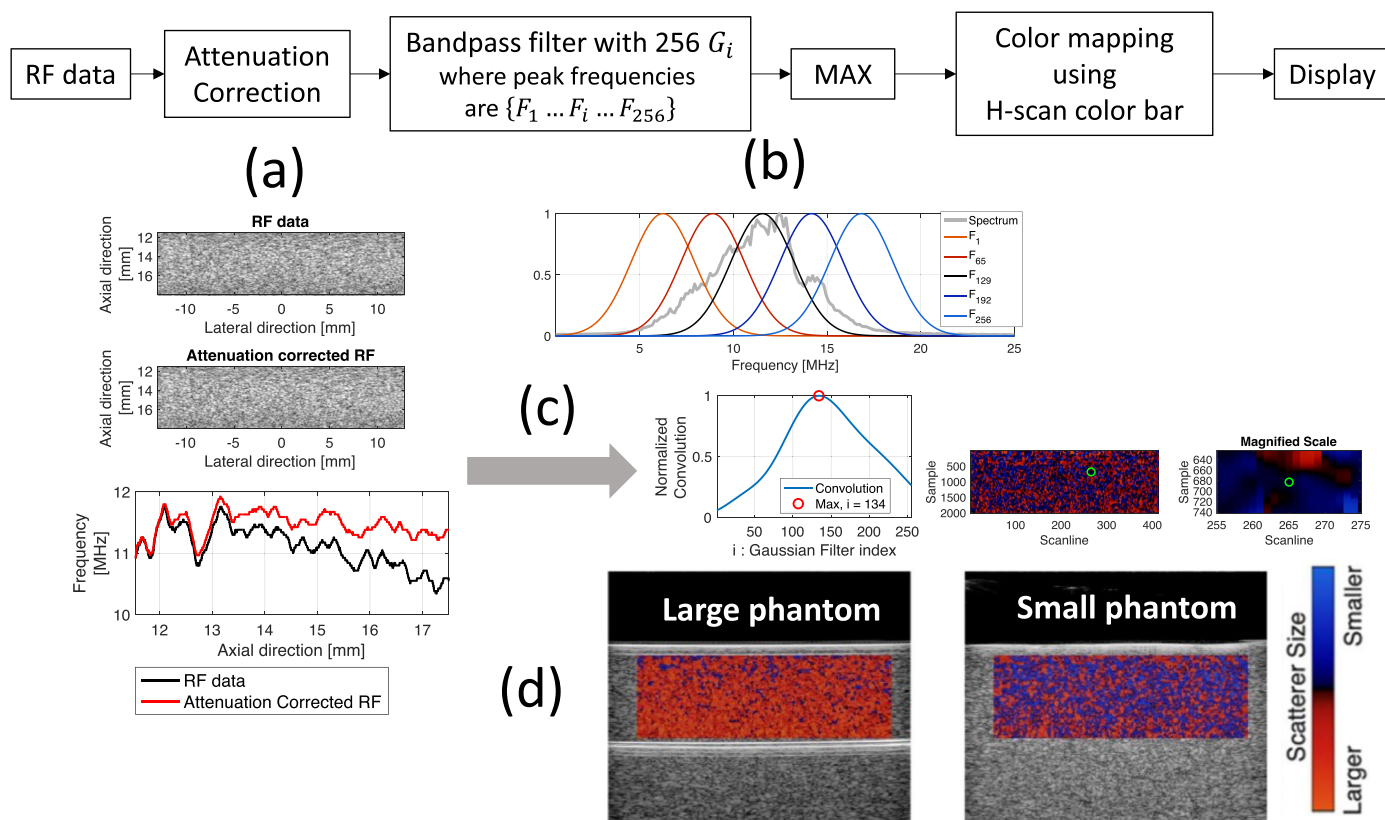
Extended Data Fig. 3 | Illustration of the H-scan algorithm. (a) Attenuation correction of the backscattered RF data is performed by dividing each ROI into 10 zones and re-incorporating the exponential decay of the backscattered power due to depth- and frequency-dependent attenuation. The dominant frequency of the backscattered signals is displayed as a function of axial depth. **(b)** A total of 256 Gaussian filters were then designed, each with a center frequency ranging from −70% to +70% of the probe center frequency of 15 MHz. **(c)** Each bandpass Gaussian filter was used on the frequency domain of the attenuation-corrected backscattered RF data at each attenuation zone. A convolution was performed with each of the 256 filters. The maximum (MAX) of this convolution was identified, and the Gaussian filter index (and corresponding color) was assigned to each depth. Frequencies lower than the center frequency were assigned red colors, and frequencies higher than the center frequency were assigned blue colors. **(d)** Representative H-scan color map display from two phantoms of different sized scatterers, denoting larger (more red) and smaller (more blue) scatterer sizes.
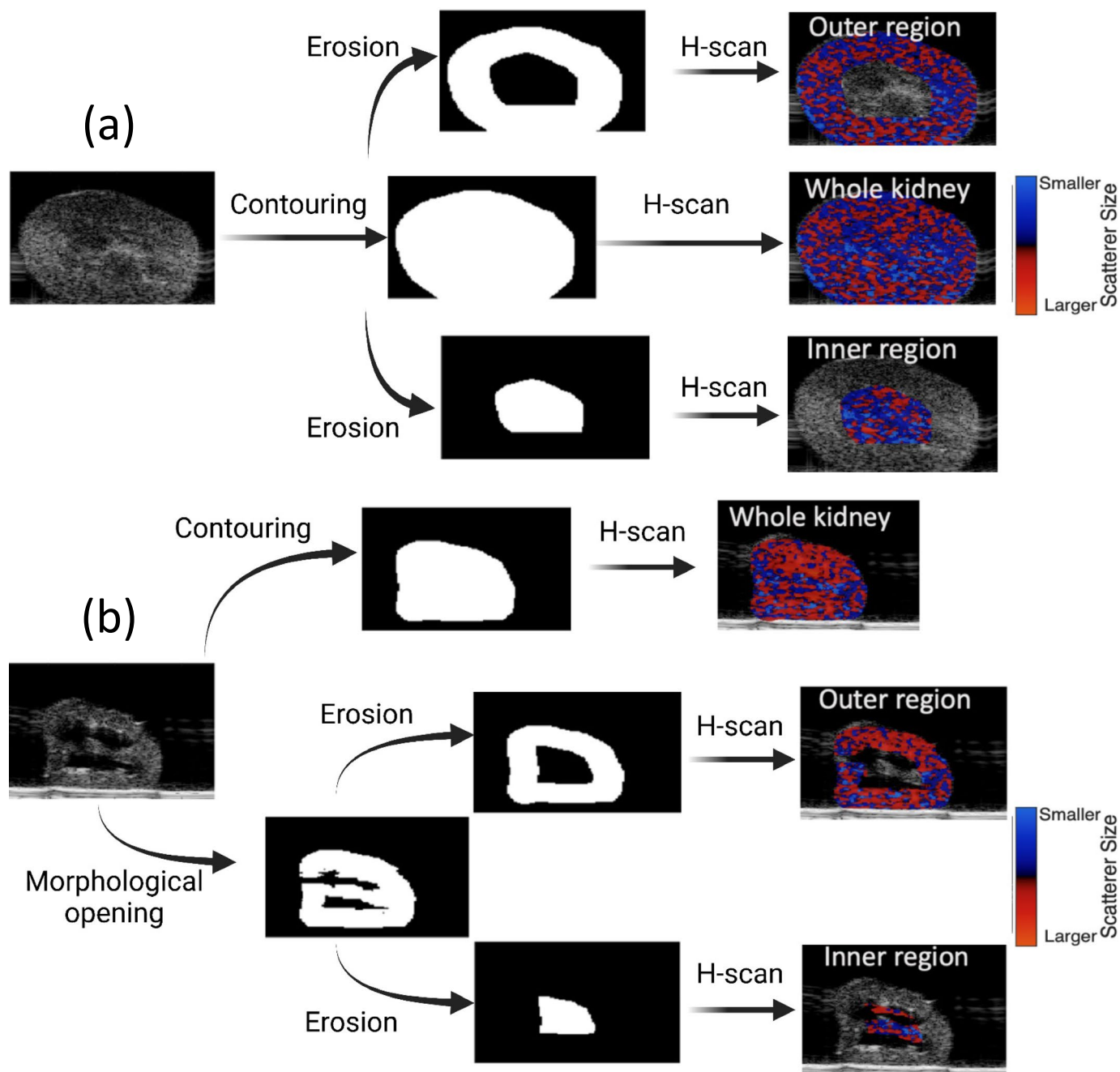
Extended Data Fig. 4 | Image preprocessing of mouse kidney H-scans.
(**a**) Normal kidneys which did not contain hypoechoic inner regions were first manually contoured. Morphological erosion was then used to separate out the outer and inner regions of the kidney. All three masks were used to perform H-scan analysis on the whole kidney, the cortex (outer region), and the medulla (inner region). (**b**) Mouse kidneys which contained inner hypoechoic regions were run through morphological opening to exclude these regions before erosion separated the cortex from the medulla. In addition, contouring was also used to segment the entire kidney. Created with BioRender.com.
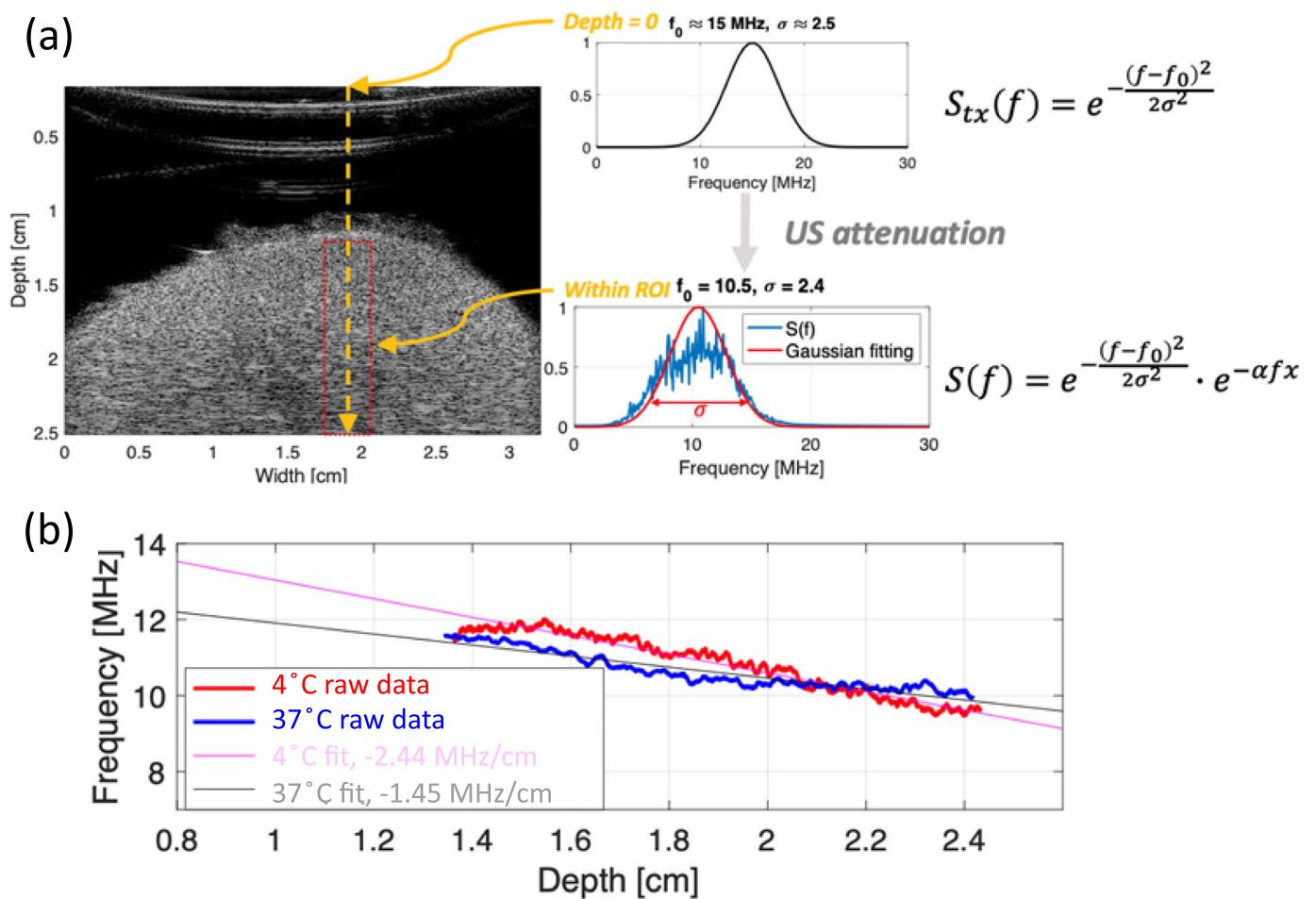
Extended Data Fig. 5 | Calculation of temperature-dependent attenuation coefficients for renal H-scan. (**a**) Schematic illustrating computation of temperature-dependent attenuation coefficients. (**b**) Peak frequency as function of depth for two temperatures relevant to the measurements of kidney transplants (*ex-vivo* on ice at 4 °C and *in-vivo* at 37 °C). The ratio between the slopes of these lines was used to obtain the attenuation coefficient at 4 °C, which was then implemented for renal H-scan estimations when imaging was performed in human donor kidneys at 4 °C.

Corresponding author(s): Darren Yuen

Last updated by author(s): Oct 31, 2024

Reporting Summary

Nature Portfolio wishes to improve the reproducibility of the work that we publish. This form provides structure for consistency and transparency in reporting. For further information on Nature Portfolio policies, see our Editorial Policies and the Editorial Policy Checklist.

Statistics

For all statistical analyses, confirm that the following items are present in the figure legend, table legend, main text, or Methods section.

n/a	Confirmed	
☐	☒	The exact sample size (*n*) for each experimental group/condition, given as a discrete number and unit of measurement
☐	☒	A statement on whether measurements were taken from distinct samples or whether the same sample was measured repeatedly
☐	☒	The statistical test(s) used AND whether they are one- or two-sided *Only common tests should be described solely by name; describe more complex techniques in the Methods section.*
☒	☐	A description of all covariates tested
☐	☒	A description of any assumptions or corrections, such as tests of normality and adjustment for multiple comparisons
☐	☒	A full description of the statistical parameters including central tendency (e.g. means) or other basic estimates (e.g. regression coefficient) AND variation (e.g. standard deviation) or associated estimates of uncertainty (e.g. confidence intervals)
☐	☒	For null hypothesis testing, the test statistic (e.g. *F*, *t*, *r*) with confidence intervals, effect sizes, degrees of freedom and *P* value noted *Give P values as exact values whenever suitable.*
☒	☐	For Bayesian analysis, information on the choice of priors and Markov chain Monte Carlo settings
☒	☐	For hierarchical and complex designs, identification of the appropriate level for tests and full reporting of outcomes
☐	☒	Estimates of effect sizes (e.g. Cohen's *d*, Pearson's *r*), indicating how they were calculated

Our web collection on statistics for biologists contains articles on many of the points above.

Software and code

Policy information about availability of computer code

Data collection	REDCap 14.0.44 was used for data collection
Data analysis	Matlab 2021a, Aperio Imagscope software v12.3.3.5048, Halo image analysis software v4.0.5107.357, R language for statistical computing v4.1.1 The code used for the H-scan algorithm is available at the following link: https://github.com/University-of-Rochester-URVentures/HScanGUI.

For manuscripts utilizing custom algorithms or software that are central to the research but not yet described in published literature, software must be made available to editors and reviewers. We strongly encourage code deposition in a community repository (e.g. GitHub). See the Nature Portfolio guidelines for submitting code & software for further information.

Data

Policy information about availability of data

All manuscripts must include a data availability statement. This statement should provide the following information, where applicable:
- Accession codes, unique identifiers, or web links for publicly available datasets
- A description of any restrictions on data availability
- For clinical datasets or third party data, please ensure that the statement adheres to our policy

Data availability statement

Research involving human participants, their data, or biological material

Policy information about studies with human participants or human data. See also policy information about sex, gender (identity/presentation), and sexual orientation and race, ethnicity and racism.

Reporting on sex and gender	Self-reported gender data was collected for both donors and recipients, and reported in aggregate in the manuscript.
Reporting on race, ethnicity, or other socially relevant groupings	Ethnicity data was collected for transplant kidney donors as this information was required to calculate the Kidney Donor Profile Index (KDPI), a measure of donor kidney quality.
Population characteristics	We collected the following data on all kidney transplant recipients: age, self-reported gender, height, weight, initial cause of end stage kidney disease, type of dialysis, dialysis vintage, and immunosuppression regimen (induction and maintenance). Similarly, we collected the following data for transplant kidney donors: age, self-reported gender, height, weight, ethnicity, history of hypertension, history of diabetes, donor type (neurological determination of death, NDD vs donation after cardiac death, DCD), cause of death, and terminal serum creatinine and Chronic Kidney Disease Epidemiology Collaboration 2021 (CKD-EPI 2021) estimated glomerular filtration rate (eGFR), and hepatitis C serology. The donor data variables were used to calculate the Kidney Donor Profile Index.
Recruitment	All patients undergoing kidney transplantation at St. Michael's Hospital between December 2021 and May 2023 were eligible and approached for recruitment into this study. Every patients was approached for consent during this time period unless logistic reasons prevented enrolment (eg. ultrasound equipment or sonographer not available).
Ethics oversight	Unity Health Toronto Research Ethics Board

Note that full information on the approval of the study protocol must also be provided in the manuscript.

Field-specific reporting

Please select the one below that is the best fit for your research. If you are not sure, read the appropriate sections before making your selection.

☒ Life sciences   ☐ Behavioural & social sciences   ☐ Ecological, evolutionary & environmental sciences

For a reference copy of the document with all sections, see nature.com/documents/nr-reporting-summary-flat.pdf

Life sciences study design

All studies must disclose on these points even when the disclosure is negative.

Sample size	As our clinical trial was a first-in-human assessment of H-scan-enabled ultrasound as a measure of kidney fibrosis, no formal sample size calculation was performed. We therefore performed a prospective cohort study aiming for an enrolment of roughly 60 donor kidneys to initially assess the diagnostic accuracy of H-scan as a measure of transplant kidney fibrosis.
Data exclusions	No data were excluded from the analyses.
Replication	For Figure 1, 5 independent human nephrectomy specimens were analyzed using H-scan and histologically via quantification of picrosirius red (PSR) and Masson Trichrome-stained sections. Each specimen was imaged at 3 different locations. Tissue sections were then obtained at each of these 3 locations, and stained with PSR and Masson Trichrome. 3 − 5 non-overlapping images were acquired from each of the PSR and Masson Trichrome stained sections, and the mean % stained area for each section was calculated. These % stained area values were then averaged, and represented in Fig. 1h-i as a mean +/- standard error of the mean (SEM) for each nephrectomy specimen. Likewise, the mean +/- SEM of the values obtained from the 3 H-scan images acquired of each nephrectomy specimen were used in Fig 1h-i.

For Figure 2, 33 living donor and 28 deceased donor kidneys were analyzed. Each kidney was stained with PSR and hematoxylin-phloxine-saffron (HPS), and 4 − 6 non-overlapping images were acquired and the % positive stained area was quantified. The average % positive stained area of these images were acquired, generating a single PSR and single HPS value for each kidney. Similarly, each kidney underwent H-scan-enhanced ultrasound of the cortex at the biopsy site, generating one value for % red H-scan pixels per kidney.

For Figure 3, the same average % positive stained PSR and HPS values from Figure 2 were used. For the % red H-scan pixel values, each kidney underwent H-scan enhanced ultrasound of (a) the cortex and medulla at the biopsy site, (b) the cortex away from the biopsy site, and (c) the cortex and medulla away from the biopsy site. Thus for each panel, a single % red H-scan pixel value was generated per kidney.

For Figure 4, the average estimated glomerular filtration rate (eGFR) for each patient was calculated from the eGFR values collected between 9 − 12 months. The number of eGFR values per patient ranged between 3 and 24.

For Figure S1e, each mouse kidney was imaged through 3 planes, and therefore each dot represents the mean % red H-scan pixel value from these 3 planes. For Figure S1f - h, each mouse kidney was sectioned through the same 3 planes, and thus each dot represents the mean (f) PSR value, (g) type 1 collagen value, and (h) alpha-smooth muscle actin value from these 3 planes. |

For Figure S5, each kidney was stained with hematoxylin-phloxine-saffron (HPS), and 4 – 6 non-overlapping images were acquired and the % positive stained area was quantified. The average % positive stained area of these images were acquired, generating a single HPS value for each kidney. Similarly, each kidney underwent H-scan-enhanced ultrasound of (a) the cortex and medulla at the biopsy site, (b) the cortex away from the biopsy site, and (c) the cortex and medulla away from the biopsy site, generating one % red H-scan pixel value per site per kidney.

Randomization	In Figure 1, a convenience cohort of 5 human nephrectomy specimens were studied, and in Figure 2, we analyzed a cohort of 61 human transplant kidneys. No allocation was required as we analyzed the ability of H-scan-enabled ultrasound to identify fibrosis when compared to gold standard histologic measurements. In Figure 4, we analyzed the estimated glomerular filtration rate (eGFR) values for a subset of 53 patients who had eGFR data available until 9 – 12 months post-transplant. No allocation was required as we analyzed the association between post-transplant eGFR at this time point with baseline H-scan-enabled ultrasound and various histologic parameters.
Blinding	All investigators were blinded during data collection and analysis.

Reporting for specific materials, systems and methods

We require information from authors about some types of materials, experimental systems and methods used in many studies. Here, indicate whether each material, system or method listed is relevant to your study. If you are not sure if a list item applies to your research, read the appropriate section before selecting a response.

Materials & experimental systems

n/a	Involved in the study
☐	☒ Antibodies
☒	☐ Eukaryotic cell lines
☒	☐ Palaeontology and archaeology
☐	☒ Animals and other organisms
☒	☐ Clinical data
☒	☐ Dual use research of concern
☒	☐ Plants

Methods

n/a	Involved in the study
☒	☐ ChIP-seq
☒	☐ Flow cytometry
☒	☐ MRI-based neuroimaging

Antibodies

Antibodies used	Mouse kidney sections were also stained with antibodies directed against alpha-smooth muscle actin (1:200 dilution, cat. no. M0851, Agilent Dako, Santa Clara, CA) or type 1 collagen (1:200, cat. no. 1310-01, Southern Biotech, Birmingham, AL).
Validation	We have used these 2 antibodies extensively to measure increases in renal myofibroblasts (alpha-smooth muscle actin) and collagen deposition (type 1 collagen) in the mouse UUO model. Please see 10.1172/jci.insight.136995, 10.1038/s41598-019-49012-4,10.1126/scitranslmed.aaz4028 as examples.

Animals and other research organisms

Policy information about studies involving animals; ARRIVE guidelines recommended for reporting animal research, and Sex and Gender in Research

Laboratory animals	6 - 8 week old C57BL/6 mice were used for our murine studies. Mice were housed in 12 hour light and 12 hour dark cycles, at a temperature of 21⬚C, and a humidity of 30 – 50%.
Wild animals	This study did not involve wild animals.
Reporting on sex	Only male C57BL/6 mice were used in these experiments. 10 male mice underwent unilateral ureteral obstruction surgery (n = 5 analyzed at day 7 post-UUO, n = 10 analyzed at day 14 post-UUO). 5 male mice underwent sham surgery (analyzed at 14 days post-surgery).
Field-collected samples	This study did not involve field-collected samples.
Ethics oversight	Murine studies were approved by the St. Michael's Hospital Animal Care Committee.

Note that full information on the approval of the study protocol must also be provided in the manuscript.

Plants

Seed stocks

Novel plant genotypes

Authentication